Dynamical analysis of early afterdepolarization patterns in a biophysically detailed cardiac model

(iD) **Roberto Barrio, M. Ángeles Martínez,** (iD) **Esther Pueyo, and** (iD) **Sergio Serrano**

View Online   Export Citation   CrossMark

ARTICLES YOU MAY BE INTERESTED IN

Scilight

Summaries of the latest breakthroughs
in the **physical sciences**

AIP Publishing

Dynamical analysis of early afterdepolarization patterns in a biophysically detailed cardiac model

Roberto Barrio,[1,a)] (ID) M. Ángeles Martínez,[1,b)] Esther Pueyo,[2,c)] (ID) and Sergio Serrano[1,d)] (ID)

AFFILIATIONS

[1] Department of Applied Mathematics and IUMA, Computational Dynamics Group, University of Zaragoza, E-50009 Zaragoza, Spain
[2] I3A, University of Zaragoza, IIS Aragón and CIBER-BBN, E-50018 Zaragoza, Spain

[a)] Author to whom correspondence should be addressed: rbarrio@unizar.es
[b)] Electronic mail: gelimc@unizar.es
[c)] Electronic mail: epueyo@unizar.es
[d)] Electronic mail: sserrano@unizar.es

ABSTRACT

Arrhythmogenic early afterdepolarizations (EADs) are investigated in a biophysically detailed mathematical model of a rabbit ventricular myocyte, providing their location in the parameter phase space and describing their dynamical mechanisms. Simulations using the Sato model, defined by 27 state variables and 177 parameters, are conducted to generate electrical action potentials (APs) for different values of the pacing cycle length and other parameters related to sodium and calcium concentrations. A detailed study of the different AP patterns with or without EADs is carried out, showing the presence of a high variety of temporal AP configurations with chaotic and quasiperiodic behaviors. Regions of bistability are identified and, importantly, linked to transitions between different behaviors. Using sweeping techniques, one-, two-, and three-parameter phase spaces are provided, allowing ascertainment of the role of the selected parameters as well as location of the transition regions. A Devil's staircase, with symbolic sequence analysis, is proposed to describe transitions in the ratio between the number of voltage (EAD and AP) peaks and the number of APs. To conclude, the obtained results are linked to recent studies for low-dimensional models and a conjecture is made for the internal dynamical structure of the transition region from non-EAD to EAD behavior using fold and cusp bifurcations and maximal canards.

Published under an exclusive license by AIP Publishing. https://doi.org/10.1063/5.0055965

In a healthy heart, the sinoatrial node sends out an electrical impulse that spreads throughout the heart activating all cardiac myocytes to produce an electrical response called the action potential (AP). The AP follows a sequence of AP phases corresponding to the inflow and outflow of ions through the membrane of cardiac myocytes. Under some circumstances, that sequence of AP phases can be disrupted by the presence of the so-called early afterdepolarizations (EADs), which are secondary voltage depolarizations that can appear during phase 2 or 3 of the AP. Side effects of drugs, ion channel dysfunction, or oxidative stress, among others, can lead to the genesis of EADs.[1–3] In heart failure, long QT syndrome, and other pathological conditions, EADs have been reported to be a relevant cause of fatal ventricular arrhythmias,[4–6] but more knowledge is required to understand the theoretical mechanisms underlying their generation. During

the last few decades, computational models of cardiac electrical activity have been instrumental in shedding light on various cardiac phenomena, including EADs. Biophysically detailed models of high dimension, i.e., with a large number of state variables, allow more faithful reproduction of experimental observations and facilitate biophysical interpretation. Here, we use the high-dimensional electrophysiological model of a rabbit ventricular myocyte developed by Sato et al.[6] with 27 state variables and 177 model parameters. By combining different techniques for dynamical system analysis, we investigate the parameter phase space using three parameters reported to highly influence model dynamics.[7] We identify regions in the phase space showing transitions from absence to presence of EADs through different temporal sequences of EADs. In these processes, dynamical phenomena are present, including bistability, chaos, fold, and cusp

bifurcations. Putting all this information together and taking into account recent findings using low-dimensional models, we provide a conjecture about the internal dynamical structure of the transition region from absence to presence of EADs in the parameter phase space studied for the Sato model.

I. INTRODUCTION

Mathematical models of biological systems have become important tools in the study of mechanisms underlying biological phenomena, complementing experimental and/or clinical research. Biological models can be very detailed (high-dimensional) and very accurate in reproducing experimental observations or they can be simple (low-dimensional) and just reproducing one or a few biological features. The former allow for more realistic interpretation of underlying mechanisms, while the latter are very useful for comprehensive theoretical studies of a particular phenomenon. The two types of models are not mutually exclusive, and they can be used synergistically to enhance modeling and simulation capabilities.

Computational models for atrial and ventricular cells in the heart (cardiomyocytes) aim at reproducing the electrical response (or action potential, AP) to an external stimulus. It is well known that, under physiological conditions, the AP responds to external stimulation by rapidly increasing the transmembrane voltage (V) in the so-called AP phase 0 (depolarization), following which there is a short transient decrease of V (transient repolarization) during AP phase 1. Next, V remains approximately constant in AP phase 2, the so-called plateau phase. During AP phase 3, V decreases (repolarization) to the resting membrane potential until the cell receives another stimulus. The time elapsed between two stimuli applied to the cell is called Pacing Cycle Length (PCL). Under some circumstances, transmembrane potential V can experience an unexpected rise during AP phase 2 or phase 3, which is termed early afterdepolarization (EAD). EADs can be produced by different causes: hypokalemia,[8,9] oxidative stress,[3] drugs,[1,8] or genetic defects.[10] If EADs at the cellular level are of large enough magnitude and occur over a substantial tissue area, they can lead to triggered activity and arrhythmias,[4,5,11–13] which makes the study of EADs highly relevant.

Many studies in the literature[14–18] investigating EADs work with low-dimensional (three, four state variables) models. For these simple models, it is common to use a fast-slow decomposition[19] approach to separate state variables that change in fast and slow timescales, respectively, thus allowing to further reduce the complexity of the system and isolate the phenomena of interest. The fast and slow subsystems can be analyzed either separately or considering the interaction between them. By using fast-slow decompositions, different dynamical mechanisms have been reported for EAD generation, ranging from a delayed subcritical Poincaré–Andronov–Hopf bifurcation[20] to folded-node singularities and their accompanying canard orbits,[16,17] finding even isolas of periodic orbits.[18] If models of higher dimension are analyzed, the mathematical tools used for low-dimensional models become increasingly difficult to apply and need to be replaced with others. One possibility for analysis is to obtain predictions using

low-dimensional models and subsequently validate them using more physiologically detailed models.[21–23]

The main goal of this work is to study the appearance of EADs in the parameter phase space of the 27-dimensional (27D) Sato rabbit ventricular cardiomyocyte model. The Sato model[6] has been widely used in the literature (both the complete model and the reduced one) and the sensitivity of its parameters has already been studied,[7] which is used here as a basis to select relevant parameters for bifurcation analysis. Due to the high number of variables and parameters of the model and the impossibility of conducting a theoretical study, we use adapted sweeping numerical techniques to study the dynamical mechanisms of EAD generation and time course. Taking into account recent findings in low-dimensional models and our results, we provide a conjecture of one possible theoretical process for EAD development in a hysteresis phenomenon. Our results agree with previous experimental and theoretical studies[8,24] showing that the frequency at which the cell is stimulated (inverse of PCL) has a major influence on EAD presence and rate of occurrence. Besides, we show the relevance of other parameters when varied in certain intervals. We report bistability, chaotic attractors, and various bifurcations. All our results correspond to the complete 27D Sato model described in Ref. 7, that is, without any reduction in the state variables or parameters of the model.

The paper is organized as follows. In Sec. II, the 27D Sato model is introduced. Section III focuses on uniparametric bifurcation analysis, both regarding EAD development (Sec. III A) and increasing rate of EAD occurrence (Sec. III B). In Sec. IV, we describe the global transformation process from the absence of EADs to all APs presenting with EADs and we define the *cardiac Devil's staircase* to explain it. In Sec. V, we expand the study to multiparametric bifurcation analysis. Section VI presents the discussion of all the obtained results as well as some theoretical conjectures. Section VII contains the conclusions of the study.

II. 27D SATO CARDIAC MODEL

In 1952, Hodgkin and Huxley[25] were the first to quantitatively describe a cell as an electrical circuit. They modeled the neuron cell membrane as a capacitor and the ion channels in it as variable conductors. Using Kirchoff's current law, the sum of the currents must be zero, that is, $I_c + I_{ion} = 0$, with I_c being the current through the capacitor and I_{ion} being the current through the conductors. The charge (Q) of a capacitor is the product of its capacitance (a constant C_m) and transmembrane potential (V). The current is the variation of charge,

$$I_c = \frac{dQ}{dt} = C_m \frac{dV}{dt}.$$

Taking into account that atrial and ventricular myocytes receive external stimulation from neighboring cells that transmit the impulse originated in the sinoatrial node, a stimulus current (I_{stim}) is introduced in the equation

$$C_m \frac{dV}{dt} = -(I_{ion} + I_{stim}).$$

Most currently existing excitable cell models are based on this Hodgkin–Huxley (HH) formalism. Models vary in complexity

depending not only on the number of ionic currents considered but also on the formulation of these currents through a number of state variables and model parameters.

In 2004, Shannon *et al.* [26] used the Hodgkin–Huxley formalism to develop a mathematical model describing major ionic currents and Ca^{2+} handling in the rabbit ventricular myocyte based on experimental evidence. Although the model was able to replicate a range of physiological properties, it failed to reproduce experimental findings for rapid heart rates, which is key for the study of cardiac arrhythmias. In 2008, Mahajan *et al.* [27] updated the model based on new available experimental data and introduced a Markovian formulation for I_{Ca} so as to replicate experimentally observed alternans in AP duration (APD) and Ca$_i$ transient (intracellular calcium concentration) at rapid heart rates. Despite those improvements, the model was still limited in reproducing EADs by increasing inward currents or decreasing outward K$^+$ currents. One year later, Sato *et al.* [6] modified the model (hereafter the Sato model) to generate EADs in a realistic way. Among others, the rate constant in the Markovian model of I_{Ca} was modified to cause steeper activation and inactivation kinetics, the maximum conductance of the L-type Ca^{2+} current was increased and the maximum conductance of I_{Ks} was reduced (see Ref. [6], supporting information, for a detailed description of changes). The Sato model used in this study is defined through 27 state variables (27D) and 177 model parameters. Specifically, we use the version of the Sato model given by Otte *et al.* [7] (see the complete description of the equations in the Appendix of that article), with a few updates to correct for minor misprints.

Next, we briefly describe the 27D Sato model, for which the total ionic current is the sum of nine ionic currents,

$$I_{ion} = I_{Ca} + I_{Na} + I_{Ks} + I_{Kr} + I_{K1} + I_{tos} + I_{tof} + I_{NaK} + I_{NaCa}.$$

An additional stimulus current, I_{stim}, is included, which is defined as a pulse of $-40\,\mu$A/cm^2 in amplitude and 1 ms in duration delivered to initiate the AP. Table I presents the nine currents together with the state variables involved in their calculation. It should be noted that calculation of, e.g., variable [Na$^+$]$_i$ depends on I_{Na}, I_{NaCa}, and I_{NaK} and calculation of c_s and c_p depends on all variables related to Ca^{2+} handling.

Sodium (I_{Na}) and potassium currents ($I_{Ks}, I_{Kr}, I_{K1}, I_{tos}, I_{tof}$) are expressed as

$$I_\xi = g_\xi \cdot \Pi_\xi \cdot (V - E_\xi), \tag{1}$$

where ξ can be Na, *Ks*, *Kr*, *K1*, *tos*, or *tof*, g_ξ is the maximum conductance of the I_ξ current, E_ξ is the Nernst potential (dependent on ion concentrations in the intracellular and extracellular spaces), and Π_ξ represents a product of gating variables and other parameters. There are 10 gating variables used in the computation of sodium and potassium currents:

- h, j, m for I_{Na};
- x_{Kr} for I_{Kr};
- x_{s1} and x_{s2} for I_{Ks};
- X_{tof}, Y_{tof} for I_{tof}; and
- X_{tos}, Y_{tos} for I_{tos}.

Each gating variable x_ξ of the sodium current is expressed as

$$\frac{d\,x_\xi}{dt} = \alpha_\xi (1 - x_\xi) - \beta_\xi \cdot x_\xi, \tag{2}$$

where x_ξ can be h, j, or m, α_ξ is the opening rate constant of gate x_ξ, and β_ξ is the closing rate constant of gate x_ξ, both of them being non-smooth (in fact, non-continuous) functions of V. As an example, for the fast Na inactivation gating variable h,

$$\alpha_h = \begin{cases} 0.135\, e^{\frac{V+80}{-6.8}}, & V < -40\,\text{mV}, \\ 0, & V \geq -40\,\text{mV}, \end{cases}$$

$$\beta_h = \begin{cases} 3.56\, e^{0.079\,V} + 31\,10^4\, e^{0.35\,V}, & V < -40\,\text{mV}, \\ \dfrac{1}{0.13\left(1 + e^{\frac{V+10.66}{-11.1}}\right)}, & V \geq -40\,\text{mV}. \end{cases}$$

An alternative form for (2) is [14]

$$\frac{dx_\xi}{dt} = \frac{x_{\xi,\infty} - x_\xi}{\tau_{x_\xi}}, \tag{3}$$

where $x_{\xi,\infty}$ is the steady-state value of x_ξ and τ_{x_ξ} is the corresponding time constant, both of them being functions of V. $x_{\xi,\infty}$ is usually a

TABLE I. Description of the nine ionic currents in the 27D Sato model.

Ionic current	Definition	Variables
I_{Ca}	The L-type Ca^{2+} current	$V, c_s, C_1, C_2, I_{1Ca}, I_{2Ca}, I_{1Ba}, I_{2Ba}, c_p$
I_{Na}	The fast sodium current	$V, m, h, j, $ [Na$^+$]$_i$
I_{Ks}	The slow component of the delayed rectifier K$^+$ current	$V, x_{s1}\, x_{s2}, $ [Na$^+$]$_i$, c_i
I_{Kr}	The rapid component of the delayed rectifier K$^+$ current	V, x_{kr}
I_{K1}	Inward rectifier K$^+$ current	V
I_{tos}	The slow component of the rapid outward K$^+$ current	V, X_{tos}, Y_{tos}, R_s
I_{tof}	The fast component of the rapid outward K$^+$ current	V, X_{tof}, Y_{tof}
I_{NaK}	The Na$^+$–K$^+$ pump current, which transports two K$^+$ ions into the cell in exchange for three Na$^+$ ions out of the cell	$V, $ [Na$^+$]$_i$
I_{NaCa}	The Na$^+$–Ca^{2+} exchanger current, which transports three Na$^+$ ions in and one Ca^{2+} ion out of the cell	$V, c_s, $ [Na$^+$]$_i$

sigmoid function, as, for example,

$$x_{Kr,\infty} = \frac{1}{1 + e^{-\frac{V+50}{7.5}}}.$$

The calcium current developed by Shannon *et al.*[26] was completed by an L-type Ca current modeled using a seven-state Markov model described in Ref. [28] and a Ca^{2+} cycling using the model of Shiferaw *et al.*[29]

Other state variables of the model include the following:

- transmembrane potential (V),
- intracellular sodium concentration $[Na^+]_i$, which is used not only in the expression of I_{Na} but also in the sodium–calcium exchanger and sodium-potassium pump currents I_{NaCa} and I_{NaK}, and
- a new variable R_s used in the expression of I_{tos}.

The remaining 14 variables are related to calcium handling and I_{Ca} current as follows:

- c_s, c_i, and c_j are the average concentrations of free Ca^{2+} in the submembrane space, cytosol, and sarcoplasmic reticulum (SR), respectively;
- c'_j is the average free Ca^{2+} concentration available for release in the junctional SR (from which Ca is transported out of the SR into the cytosol);
- c_p is the average Ca^{2+} concentration in active dyadic clefts;
- J_{rel} is the total release flux out of the SR via ryanodine receptor channels;
- C_1, C_2, I_{1Ca}, I_{2Ca}, I_{1Ba}, and I_{2Ba} are L-type Ca^{2+} channel states; and
- $[CaT]_i$ and $[CaT]_s$ are concentrations of Troponin C binding sites.

Regarding model parameters, 30 are related to Na^+, 61 are related to K^+, 60 are related to Ca^{2+} distributed in five groups [SR release (8), cytosolic buffering (13), uptake and SR leak (4), I_{Ca} current (14), and other constants (21)], 15 are related to exchanger and pump currents, and finally, 11 are physical constants and ionic concentrations.

From the above, it can be observed that the 27D Sato model is a highly detailed model with non-smooth functions, non-linearities, high dimension, and a large number of parameters. Here, the system of 27 ordinary differential equations was solved in C^{++} using an embedded Runge–Kutta formula [Dormand-Prince RK5(4)] with variable stepsize. The error tolerance was set to 10^{-8} with a minimum time step of 0.002 ms. The complete set of initial conditions for most of the simulations is presented in Table II.

III. TRANSITIONS TO EADs

Figure 1 shows several time series of transmembrane potential V when pacing the cardiomyocyte at different *PCLs*. At low *PCL* (1100 ms), no EAD is observed. For increasing *PCLs*, a larger number of APs with EADs appear and it is possible to locate orbits where there is an AP without an EAD and other AP with an EAD. At high *PCL* (1400 ms), all APs show an EAD. In this figure, K_{mNao} and K_j have the default values in the Sato model (87.5 mM and 50 μM, respectively). The shaded region in Fig. 1 indicates the periodic behavior for each configuration.

TABLE II. State variables of the model and their initial conditions, as in Ref. 7.

Ion	Variable	Initial value
Ca^{2+}	c_s	$0.137\,483\,\mu$M
	c_i	$0.130\,489\,\mu$M
	c_j	$127.498\,\mu$M/1 cytosol
	c'_j	$125.711\,\mu$M/1 cytosol
	c_p	$0.597\,462\,\mu$M
	J_{rel}	$0.004\,609\,1\,\mu$M/ms
	C_1	$1.365\,21 \times 10^{-6}$
	C_2	$0.991\,324$
	I_{1Ca}	$3.328\,17 \times 10^{-7}$
	I_{2Ca}	$1.430\,69 \times 10^{-5}$
	I_{1Ba}	$5.283\,78 \times 10^{-7}$
	I_{2Ba}	$0.008\,659\,14$
	$[CaT]_i$	$12.7657\,\mu$M/1 cytosol
	$[CaT]_s$	$13.2176\,\mu$M/1 cytosol
Na^+	$[Na^+]_i$	10.0799 mM
	h	$0.991\,187$
	j	$0.994\,21$
	m	$0.001\,033\,12$
K^+	x_{Kr}	$0.006\,776\,89$
	x_{s1}	$0.011\,933\,9$
	x_{s2}	$0.066\,408\,3$
	$X_{to,f}$	$0.003\,585\,45$
	$Y_{to,f}$	$0.995\,458$
	$X_{to,s}$	$0.003\,585\,75$
	$Y_{to,s}$	$0.297\,391$
	R_s	$0.417\,681$
	V	-87.4094 m V

In the following, the Farey sequence notation L^s, taken from the mixed-mode oscillations (MMOs) literature,[30] is adopted to characterize the periodic orbits with large –L– and short –s– oscillations. 1^0 means an AP without EAD and 1^1 an AP with an EAD. All our periodic orbits have sequences of these two kinds of APs. As an example, the sequences corresponding to the periodic orbits of Fig. 1 are 1^0, $1^0 1^1$, $1^0 (1^1)^2$, $1^0 (1^1)^3$, and 1^1, respectively.

To study the evolution between the different sequences shown in Fig. 1, we calculated a bifurcation diagram for the range of investigated *PCLs*. To build bifurcation diagrams, we departed from a *PCL* value (all other model parameters have default values as in Ref. 7) and the initial conditions shown in Table II. We integrated an initial transient time (a given number of APs), following which we continued the integration to find a periodic orbit. Throughout this study, to check if an orbit was periodic, each time a main peak was detected, we evaluated whether the difference between this peak and any of the previously detected ones was lower than 10^{-5} mV in the transmembrane potential, V, and 10^{-5} mM in the intracellular $[Na^+]_i$ concentration. If detected, integration was performed until the final part of the AP (since the periodicity algorithm used the peaks for evaluation) and the integration was stopped. If a periodic orbit could not be detected, the integration stopped when reaching a maximum number of APs. To subsequently reproduce the orbits, the
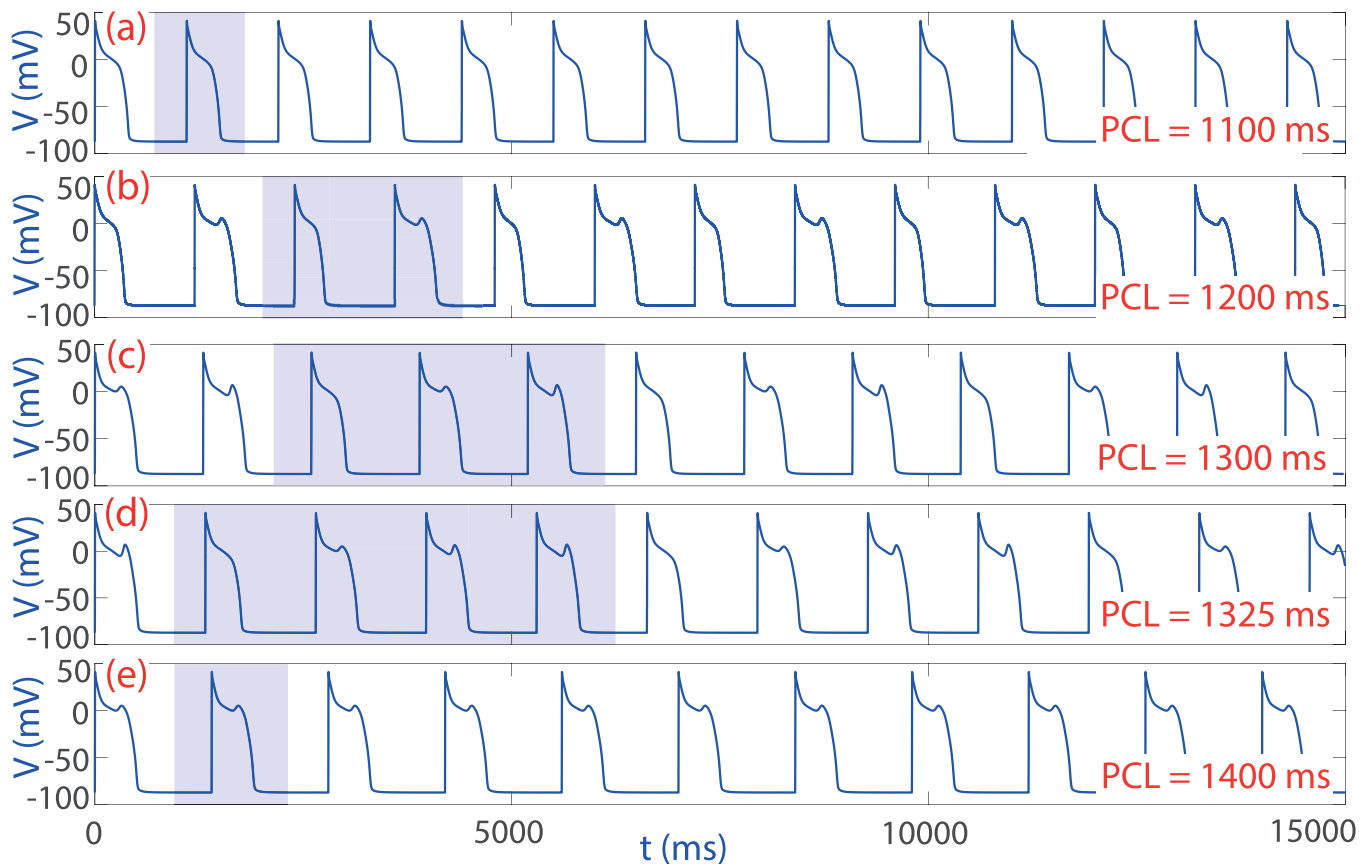
FIG. 1. Membrane voltage V for different PCL values. (a) At low PCL (1100 ms), no EAD is observed. For increasing $PCLs$, a larger number of APs with EADs appear: (b) one every two APs with EAD ($PCL = 1200$ ms), (c) two every three APs with EAD ($PCL = 1300$ ms), (d) three every four APs with EAD ($PCL = 1325$ ms), and so on. (e) At high PCL (1400 ms), all APs present an EAD. Shaded regions show the periodic behavior.

PCL value, the number of APs, the number of peaks (both AP peaks and EAD peaks), the values of state variables at those peaks, and the final values taken by the 27 state variables were recorded. Next, the following PCL value was analyzed, taking as initial conditions the values of the state variables at the end of the last integration and the procedure was repeated. The initial transient time was longer than the transient time applied to subsequent $PCLs$. The same procedure could be applied using other parameters rather than PCL. Figure 2 shows the results for $PCL \in [1100, 1400]$ ms, applying a transient time of 200 APs.

Blue points in Fig. 2 represent the value of V for the AP peaks (≈ 40 mV) at the top and the EAD peaks (≈ 8 mV) at the bottom. In contrast to other studies[7,17] that used the APD to build the bifurcation diagram, we represent the transmembrane potential at the peaks (either AP or EAD peak) to have more information about the AP behavior. In the bifurcation diagram of Fig. 2, we marked three colored areas. The white area on the left corresponds to APs without EAD, with sequence 1^0, for which no EAD peaks appear

in the bottom part of the figure. The clear blue area corresponds to alternations of APs with EADs and APs without EADs. The clear green area represents $PCLs$ for which all APs show an EAD, that is, sequence 1^1.
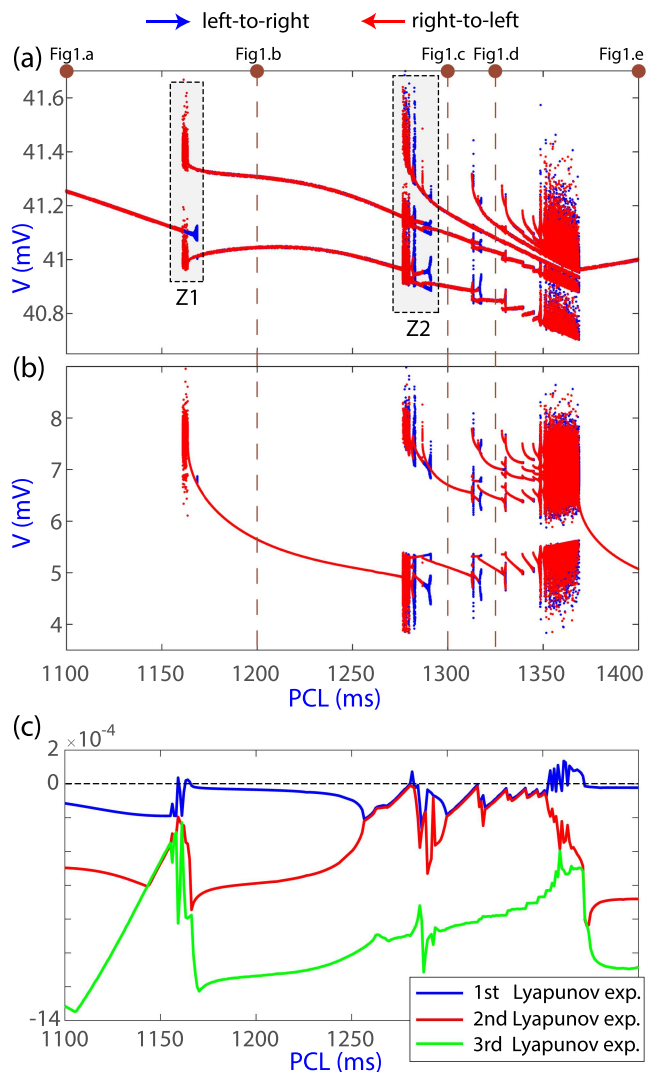
Brown points at the top of Fig. 2 correspond to the PCL values of the time series shown in Fig. 1: $PCL = 1100$ ms (AP without EAD), $PCL = 1200$, 1300, and 1325 ms (APs with and without EADs), and $PCL = 1400$ ms (all APs with an EAD). To better appreciate the structure of the top and bottom parts of the diagram corresponding to AP and EAD peaks, respectively, Fig. 3 presents a magnification of the bifurcation diagram for both regions [AP peaks in panel (a) and EAD peaks in panel (b)]. Additionally, the bifurcation diagram is presented in two different continuation ways. Blue points correspond to increasing PCL starting from $PCL = 1100$ ms, while red points correspond to decreasing PCL starting from $PCL = 1400$ ms. Those regions where both colors are visible represent coexistence of attractors, that is, starting from different initial conditions, the system can experience different behaviors for the
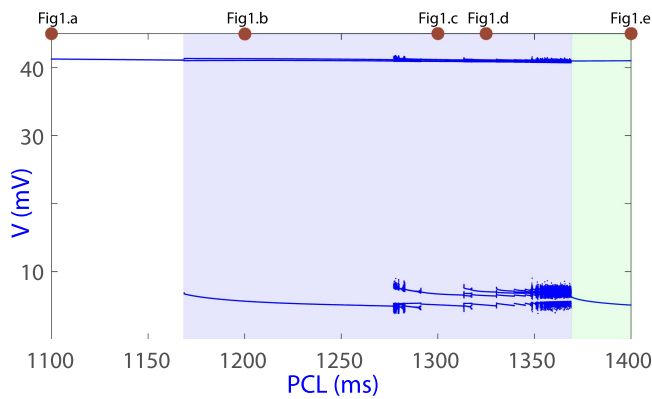
FIG. 2. Bifurcation diagram for varying *PCL*. The blue points at the top part of the bifurcation diagram correspond to AP peaks ($\approx$41 mV) and those at the bottom part to EAD peaks ($\approx$8 mV). The white area represents APs without EADs. The brown point at the top of the panel in the white area corresponds to $PCL = 1100$ ms, for which the temporal sequence is plotted in the first panel of Fig. 1. The clear blue area represents alternating sequences of APs with and without EADs. The three brown points correspond to $PCL = 1200$, 1300, and 1325 ms, respectively, plotted in Fig. 1. The clear green area corresponds to *PCL* values, for which all APs show an EAD. The brown point corresponds to $PCL = 1400$ ms, and it is plotted in the last panel of Fig. 1.

FIG. 3. Panel (a) shows the main AP peaks (upper branches of Fig. 2) and panel (b) shows the EAD peaks (lower branches of Fig. 2). Blue points are obtained for increasing *PCL* values (from left to right) and red points for decreasing *PCL* values (from right to left). In (a), zone Z1 corresponds to the change from absence to presence of EADs (transition from 1^0 to $1^0 1^1$), while zone Z2 corresponds to the addition of another AP with EAD to the periodic orbit [transition from $1^0 1^1$ to $1^0 (1^1)^2$]. Panel (c) shows the first three Lyapunov exponents along the *PCL* range.

same parameter values. Note that this bistability is relevant in biology, as both attractors may have completely different behaviors and it may be of interest to avoid some of them.

Panels 3(a) and 3(b) present similar structures. Limited by transition regions where the number of EADs augments, the diagram is divided into several intervals corresponding to basic periodic orbits illustrated by the first four (from the left) top brown points. In these intervals, it is possible to observe the lines associated with each AP in panel (a) and with each EAD (one less) in panel (b). All these orbits have a sequence of the type $1^0 (1^1)^n$, starting with $n = 0$ (that is, the sequence 1^0) in the left area (around $PCL = 1100$ ms) and increasing the value of n until reaching the last area (around $PCL = 1400$ ms) with sequence 1^1. In all of them, the upper branches correspond to the AP without EAD, while all the others are APs with an EAD. It can be noted that there is one less branch in panel (b) than in panel (a) for all analyzed *PCL* areas except for the last one, where all APs have an EAD. From panel (b), it can be seen that the more APs with EADs, the higher the amplitude of those EADs. This can also be appreciated in the time series of Fig. 1. Also from this figure, it is possible to observe that there are transition regions with coexistence of attractors and chaotic behavior. The first two transition zones, marked Z1 and Z2 in panel (a), will be studied in more detail in Subsections III A and III B. In panel (c), the first three Lyapunov exponents, calculated with the algorithm proposed in Ref. 31, are shown, which confirm the existence of areas with stable behavior and others with chaotic behavior, in line with the previously published results.[7] For increasing *PCL*, the size of the different sections becomes smaller, making it more difficult to distinguish one from the other until reaching the limit of the 1^1 sequence with all APs having an EAD.

A. The emergence of EADs: From non-EAD to alternans

This subsection focuses on the analysis of the first transition zone in Fig. 3, marked as Z1, where model dynamics changes from an orbit with an AP without EAD, with sequence 1^0, to another orbit with two APs, one without EAD and another one with an EAD, sequence $1^0 1^1$, that is, presenting AP alternans.[32–34]
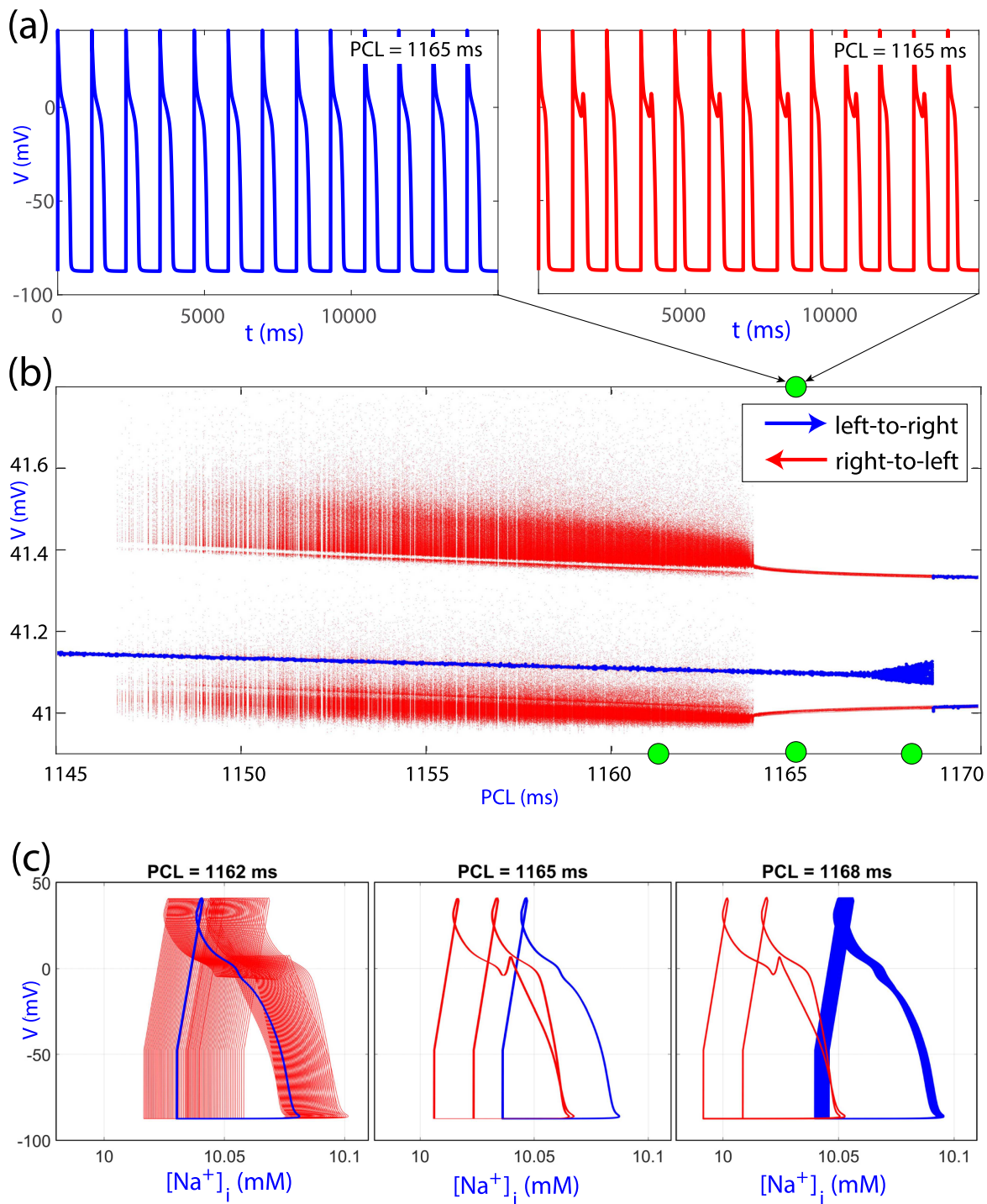
FIG. 4. (a) Time series obtained for $PCL = 1165$ ms with different initial conditions showing the two coexisting stable APs. For the left orbit (in blue), there are no EADs, while for the right orbit (in red) there is an EAD every two APs. (b) Magnification of the first transition region Z1 of Fig. 3(a). Blue points and orbits are obtained for increasing PCL values (from left to right) and red points for decreasing PCL values (from right to left). (c) Representation of V vs $[Na^+]_i$ for the three PCL values selected in panel (b). Important differences can be observed as coexisting periodic orbits and chaotic or torus attractors.
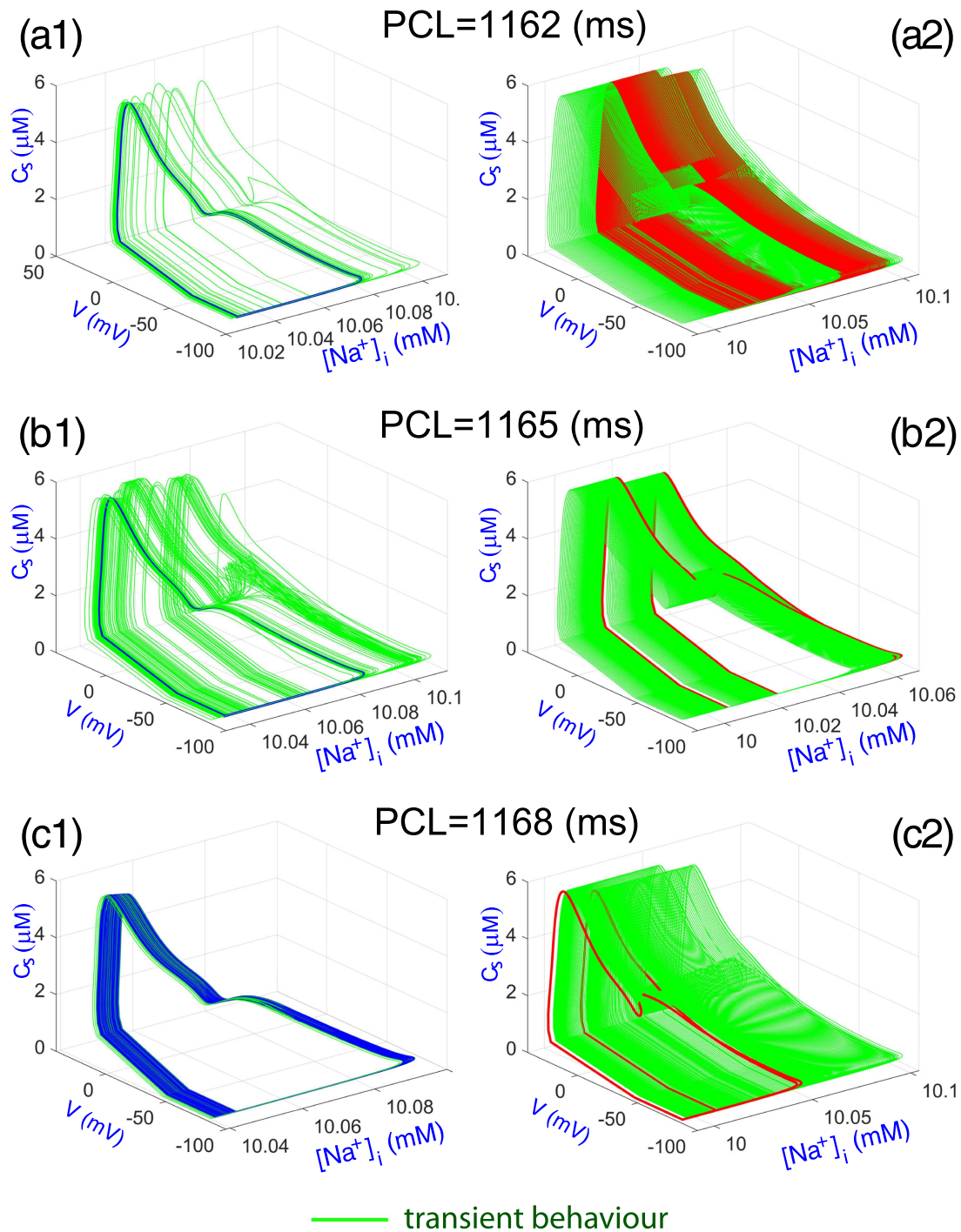
FIG. 5. Representations of C_s vs V vs $[Na^+]_i$ for the three *PCL* values [(a1) and (a2) *PCL* = 1162 ms, (b1) and (b2) *PCL* = 1165 ms, and (c1) and (c2) *PCL* = 1168 ms] selected in Fig. 4 (green points). Starting from different initial conditions and after a transient time (in green), trajectories will fall into the different attractors (in red and blue) shown in Fig. 4. In (c1), the basin of attraction is very small; thus, initial conditions very close to the torus are required so that the trajectory ends up falling into it.

Figure 4, panel (b), presents a magnification of zone Z1 from Fig. 3(a) where the transition from non-EAD to EAD is shown for the same two initial condition strategies as in Fig. 3. On the left side of the figure, there is a periodic attractor (in blue) formed by an AP without EAD. In contrast, on the right side, the periodic attractor (in red) comprises two APs, one with an EAD and the other one without an EAD ($1^0 1^1$ orbit). In the intermediate region, the coexistence of different attractors is detected. The top panels in (a) show two temporal series for $PCL = 1165$ ms obtained with different initial conditions. The left orbit (blue) does not have any EAD; however, the right orbit (red) has one EAD every two APs. They represent the standard periodic orbits (out of the transition region) in this PCL interval. A 2D projection presenting V vs $[Na^+]_i$ is shown in the central graph of panel (c), where two coexisting stable periodic orbits can be seen. If the orbit without EADs (in blue) is analyzed for higher PCL values (to the right), the periodic orbit can be observed to undergo a bifurcation and appears to turn into a torus. The right plot of panel (c) shows this attractor (for $PCL = 1168$ ms), with still no EADs, coexisting with the periodic orbit of type $1^0 1^1$ (in red). On the other hand, if lower values of PCL are analyzed, the attractor without EADs is still periodic, while the attractor with EADs is no longer periodic but chaotic. The left plot of panel (c) shows this chaotic attractor for $PCL = 1162$ ms coexisting with the periodic orbit 1^0. The main sequence of this chaotic attractor is still $1^0 1^1$, but from time to time (without a defined pattern) several APs without EADs appear. Note that the coexistence of both families of attractors (without EAD and with EAD), together with the fact that the periodic attractor without EADs (blue line) becomes a torus-type attractor (for which alternans arise), make us conjecture that both stable branches are connected by an unstable branch along which one type of orbit passes into the other one through some bifurcations, as commented in the Discussion section.

The region of coexistence shown in Fig. 4 will probably be larger than the one detected, as the computed bifurcation diagrams depend on the size of the basins of attraction. In fact, in Fig. 3, there is a smaller coexistence region than in Fig. 4 because the basins of attraction become smaller at the ends of the coexistence interval. In Fig. 4, it has been possible to continue both attractors for a larger interval because of a smaller step size when varying PCL was taken so that the attractors for two consecutive PCL values are very similar. Therefore, starting from initial conditions associated with the previous attractor, the orbit ends up falling into the same type of attractor for the new PCL value. This can also be observed in Fig. 5, where trajectories computed from different initial conditions are shown. The transient orbits are not removed from the plots but are shown in green. For the three PCL values selected in Fig. 4, the initial conditions given in Table II were considered. For $PCL = 1162$ ms and $PCL = 1165$ ms, the trajectory ends at the blue periodic attractor 1^0 (a1) and (b1), respectively. However, for $PCL = 1168$ ms, the trajectory ends at the red periodic orbit $1^0 1^1$ (c2). Thus, some time after starting with the same initial conditions of Table II, the trajectory can happen to range from being in the basin of attraction of the attractor 1^0 to being in the basin of the attractor $1^0 1^1$, depending on the PCL value.

For other initial conditions, trajectories can end up falling into other attractors. For the chaotic attractor and periodic orbit in red with $PCL = 1162$ ms and $PCL = 1165$ ms [panels (a2) and (b2)],
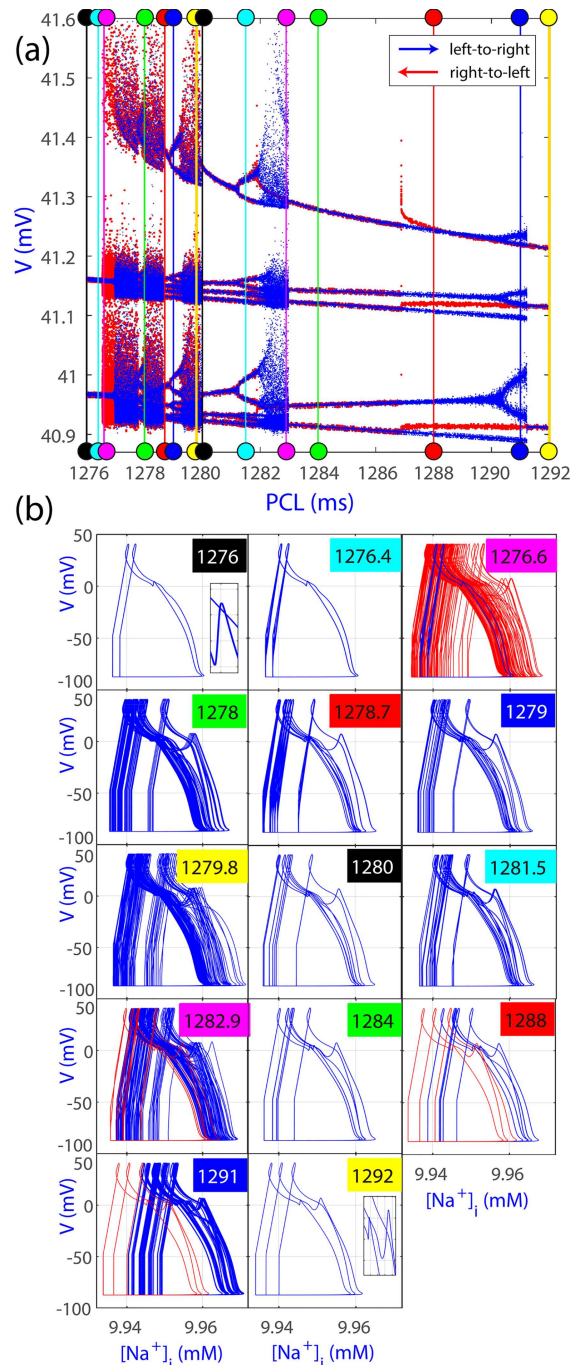

FIG. 6. (a) Bifurcation diagram for transition zone Z2 from Fig. 3(a), going from a periodic orbit with two APs (one with EAD), sequence $1^0 1^1$, to a periodic orbit with three APs (two of them with EADs), sequence $1^0 (1^1)^2$. In the middle of the PCL interval, there are regions of coexistence of chaotic and regular behaviors originated by various bifurcations. (b) The attractors for 14 PCL values exhibiting different behaviors (100 APs are plotted for each orbit). In coexistence cases, the two attractors are shown in blue and red.
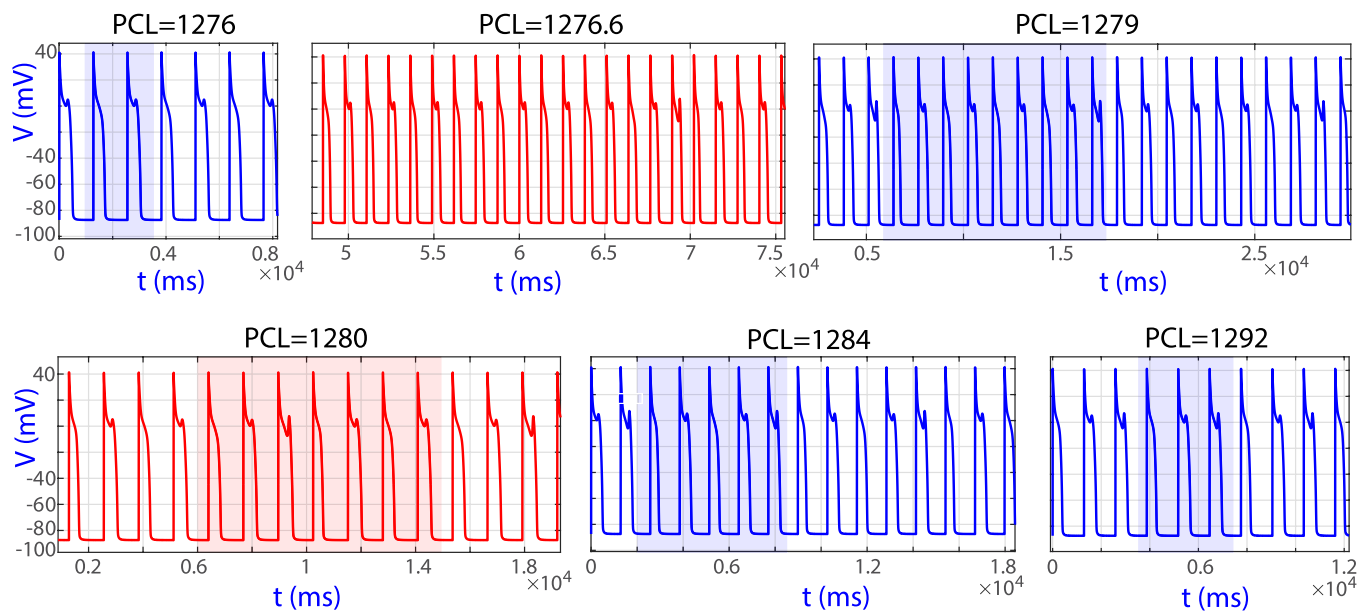
FIG. 7. Time series for some selected attractors of Fig. 6(b), ranging from $PCL = 1276$ ms, with a periodic orbit $1^0 1^1$, to $PCL = 1292$ ms, with a periodic orbit $1^0 (1^1)^2$, through different intermediate states illustrating the transition.

respectively, initial conditions can be defined by taking the values of the state variables at a point of the attractor $1^0 1^1$ for a different PCL value. However, for the torus orbit (in blue) that appears for $PCL = 1168$ ms, starting from initial conditions very close the torus is required to end up falling into it, as otherwise the periodic orbit $1^0 1^1$ will end up being reached, which means that the basin of attraction for the torus orbit (c1) is very small.

As a final observation from Fig. 5, it is possible to monitor the trajectory followed by the system, starting from initial conditions outside an attractor and converging into it. We have selected as PCL values the green points highlighted in Fig. 4. In all cases, the trajectories (transient or not) can be seen to exhibit similar APs forming tubular structures, sometimes converging later to a periodic orbit or to a smaller tubular structure. The main difference is that some tubular structures have EADs, so there are two underlying tubular manifolds.

B. Increasing the presence of EADs

This subsection analyzes the second transition zone, marked as Z2 in Fig. 3(a), which is actually composed of several consecutive transitions, as illustrated in Figs. 6 and 7. Figure 6(a) shows the bifurcation diagram of zone Z2, and Fig. 6(b) presents 2D projections of the attractors for various PCL values corresponding to the color dots in the bottom bar of plot (a). The time series associated with some of these attractors are shown in Fig. 7, with shaded areas indicating the basic pattern of these series.

Starting with the lowest PCL value in Fig. 6, $PCL = 1276$ ms, the only attractor is still the periodic orbit $1^0 1^1$ that already appeared in the right part of zone Z1, which has been the only attractor in

all the intermediate region of Fig. 3. For slightly higher PCL values, approximately (1276.5 and 1278.7 ms), a chaotic attractor appears in the red orbit, initially coexisting with the previous periodic orbit in blue. For this interval, some short windows of stability are observed and there are likely many more not visible. Following the chaotic path, after some sequences of the type $(1^0 1^1)^n$, a sequence $1^0 (1^1)^2$ appears, as can be appreciated in the second panel of Fig. 7 ($PCL = 1276.6$ ms), but without any periodicity. For higher PCL values, a stability window can be observed, starting at $PCL \simeq 1278.7$ ms, with a periodic orbit $(1^0 1^1)^3 1^0 (1^1)^2$ that subsequently experiences a period-doubling cascade to chaos, where sequences $(1^0 1^1)^3 1^0 (1^1)^2$ are followed by sequences $(1^0 1^1)^2 1^0 (1^1)^2$ without a periodicity pattern. For even higher PCL values, the chaotic attractor becomes a saddle invariant set and no more an attractor, $PCL \simeq 1280$ ms, and a periodic orbit with sequence $(1^0 1^1)^2 1^0 (1^1)^2$ is the only attractor detected. The process continues in a similar way as before, but now the chaotic attractor combines sequences $(1^0 1^1)^2 1^0 (1^1)^2$ with sequences $(1^0 1^1) 1^0 (1^1)^2$. In this case, even before reaching the region with chaotic behavior ($PCL \simeq 1282$ ms), the appearance of a periodic attractor $(1^0 1^1) 1^0 (1^1)^2$ can be observed to coexist with the previous attractor throughout the process above described. From $PCL \simeq 1283$ ms, the chaotic attractor becomes again a saddle invariant set and the periodic orbit $(1^0 1^1) 1^0 (1^1)^2$ is the only attractor until $PCL \simeq 1287$ ms, where a new stable periodic orbit, $1^0 (1^1)^2$, appears and coexists with it. Next, the periodic orbit $(1^0 1^1) 1^0 (1^1)^2$ begins an incomplete period-doubling cascade ($PCL \simeq 1291.2$ ms). What has probably happened is that the attractor has undergone a basin metamorphosis bifurcation[35] whereby its basin of attraction has greatly reduced its size and shape abruptly, so it is not possible to track it.

In any case, at that time or slightly later, the periodic orbit $1^0(1^1)^2$ becomes the only attractor along an interval around the value of $PCL = 1300$ ms [see Figs. 1(c) and 3(a)].

Note that, as it was the case in zone Z1, the coexistence intervals are probably longer, but the basins of attraction are too small to be identified. Exactly locating these intervals is not the objective of this article, which aims at providing a global view of the process of EAD generation. Also, the complexity of the dynamics that coexist makes it difficult to rigorously ensure that the detected orbits are periodic and, if they are, their exact multiplicity. For this reason, we have preferred to give the basic sequence observed both in the bifurcation diagram and with the time series.

The following transition is from the periodic orbit with three APs, $1^0(1^1)^2$, to the periodic orbit with four APs, $1^0(1^1)^3$ (see Fig. 1) at around $PCL = 1320$ ms. Transitions continue until the final state with EADs in all APs (1^1) is reached.

IV. LIMIT TO THE CONTINUOUS EAD: THEORETICAL SCHEME OF THE TRANSITION PROCESS

In Sec. III, the evolution of the system dynamics when PCL varies from 1100 to 1400 ms was described, going from a periodic orbit without EADs to another periodic orbit where all APs have an EAD. In between, there are regions with periodic orbits in which some APs have EADs and others do not, being these regions separated by transition zones where chaotic behavior and various bifurcations appear. This section focuses on the periodic orbits to study the global transformation process while providing its symbolic description for better understanding (note that the use of symbolic analysis provides powerful techniques in various fields, such as neuron models[36]). The transitions studied in zones Z1 and Z2 are shown to be two steps of the same "staircase" process and the transition described in Z2 is shown to obey a generic pattern that "builds" the intermediate steps.

To describe this symbolic evolution, we use the symbolic sequences of the periodic orbits and the ratio between the number of peaks (both AP and EAD peaks) and the number of APs of the same orbits. Tables III and IV show examples of both notations. When a periodic orbit is found, the total number of peaks (i.e., AP and EAD peaks) in the periodic orbit and the number of APs (i.e., main peaks) are counted. Figure 8(a) shows (in magenta and gray) the ratio between both values for all the periodic orbits detected in the interval $PCL \in [1100, 1400]$ ms. Although this ratio does not detect if an orbit undergoes a period-doubling bifurcation, here we just focus on the basic sequences, which can be repeated several times in the actual periodic orbits. From Fig. 8(a), an ascending staircase toward the continuous EAD case (1^1 orbit) can be appreciated. This is called a Devil's staircase-like structure[37] in the literature, which for this case we term as *cardiac Devil's staircase*. Similar figures

can be found in other studies,[8,38,39] but here we identify the Devil's staircase and complement it with symbolic sequences to detect the patterns that generate it. From these staircase and previous bifurcation diagrams, it is clear that an increase in PCL implies a higher number of APs with EADs, as shown in previous experimental and computational investigations.[8,40]

From Fig. 8(a), some steps can be seen to be larger than those around them. We term these steps as primary steps (plotted in magenta) and the rest (plotted in gray) as secondary steps. Panel (a) contains the complete staircase from 1^0 to 1^1, while panel (b) offers a magnification of the upper steps. For each basic periodic orbit, the time series is plotted in blue and the corresponding sequence is shown in a box. As can be seen from the figure, all the primary steps correspond to sequences that fit into the generic pattern $1^0(1^1)^n$, being the first step the case $n = 0$ and being the last one the limit case 1^1. Moreover, if a primary step has the sequence $1^0(1^1)^n$, the next primary step corresponds to the sequence $1^0(1^1)^{n+1}$, that is, the next primary step has a periodic orbit with one AP more than the previous one. In all these orbits, only one AP does not have EAD while the rest do. These steps well match the zones corresponding to the basic periodic orbits identified in the bifurcation diagram of Fig. 3 (some of them marked by dashed brown vertical lines associated with brown dots), where the AP without EAD is represented in the bifurcation diagram by the highest section of that orbit, as previously described. The information corresponding to the primary steps converging toward the limit case is summarized in Table III, where the symbolic sequence, the number of peaks/number of APs, and the ratio between these two numbers are shown.

Between every two primary steps, secondary steps are detected, except for between the first and second steps, which corresponds to the transition zone Z1 represented in Figs. 3 and 4. Here, no periodic orbit with intermediate state between the first and the second primary steps is detected. This does not mean such orbits do not exist, but stability windows can be very small and difficult to find. Panel (c) shows an enlargement of the second jump between primary steps, which corresponds to the transition zone Z2. Going from top to bottom, secondary steps with symbolic sequence $(1^01^1)^n1^0(1^1)^2$ can be observed, with $n = 1$ for the first secondary step and n increasing as going down in the staircase. Note that this sequence is formed by the combination of n repetitions of 1^01^1, corresponding to the lower primary step, and a repetition of $1^0(1^1)^2$, corresponding to the upper primary step. As mentioned in the previous section, the first four secondary steps were located, but there are certainly more stability windows, smaller in size, in which lower steps appear. We conjecture that there will be infinite windows whose limit (with $n \to \infty$) will be the stability window with periodic orbit of sequence 1^01^1. This information is summarized in Table IV. In the following secondary steps, the same pattern is observed with sequences

TABLE III. Sequences of periodic orbits forming the primary steps with increasing number of APs with EADs shown in Fig. 8.

Name	1^0	$1^0(1^1)$	$1^0(1^1)^2$	$1^0(1^1)^3$	$1^0(1^1)^4$	$1^0(1^1)^5$	$1^0(1^1)^6$	⋯	$1^0(1^1)^n$	⋯	1^1
Peaks/APs	1/1	3/2	5/3	7/4	9/5	11/6	13/7	⋯	(2n+1)/(n+1)	⋯	2/1
Ratio	1	1.5	1.67	1.75	1.8	1.83	1.86	⋯	2-1/(n+1)	⋯	2

TABLE IV. Sequences found in the transitions from a two-AP periodic orbit to a three-AP periodic orbit, as shown in Figs. 6 and 8.

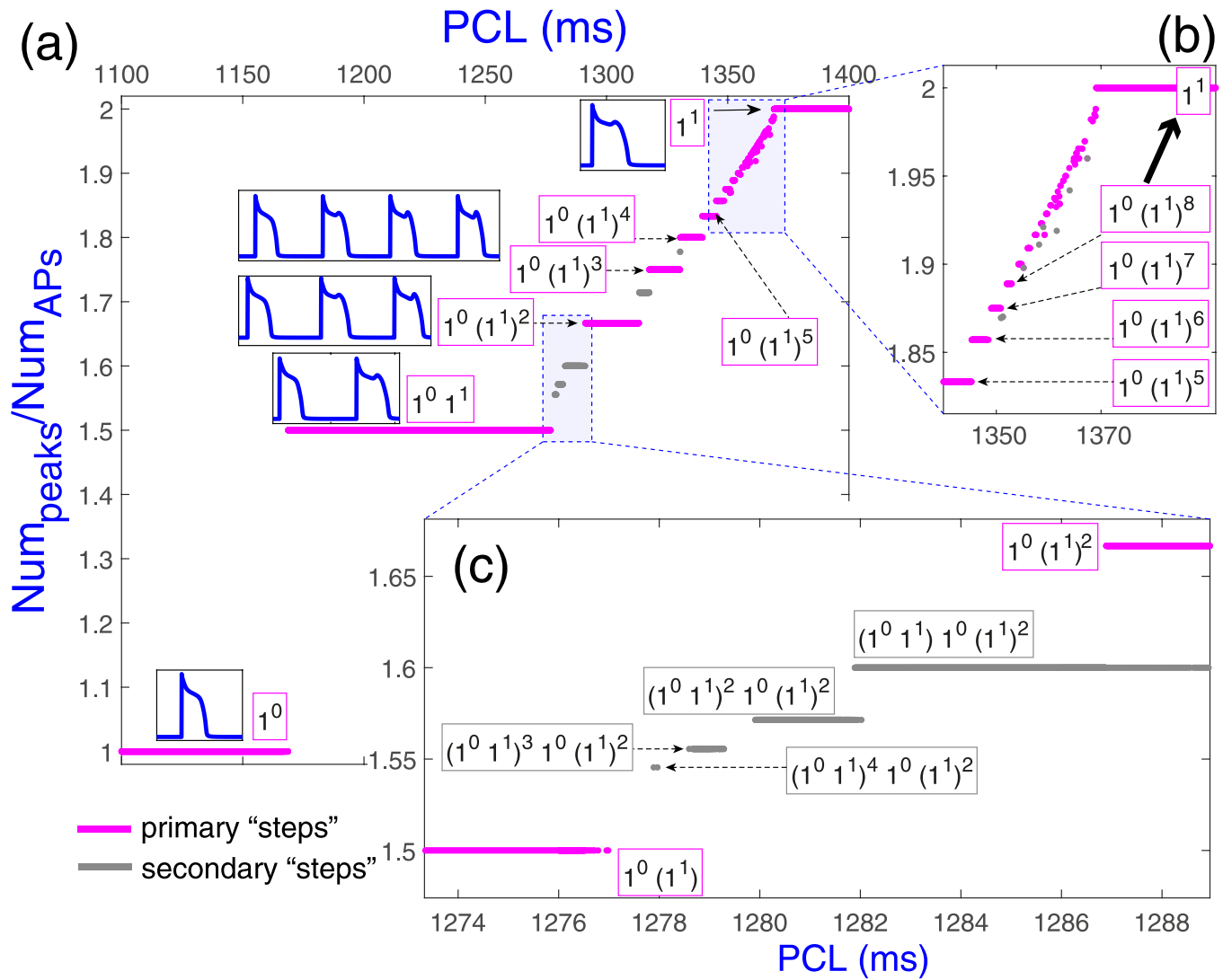| Name	$1^0 (1^1)$	$\cdots$	$(1^0 1^1)^4 1^0 (1^1)^2$	$(1^0 1^1)^3 1^0 (1^1)^2$	$(1^0 1^1)^2 1^0 (1^1)^2$	$(1^0 1^1) 1^0 (1^1)^2$	$1^0(1^1)^2$
Peaks/APs	3/2	$\cdots$	17/11	14/9	11/7	8/5	5/3
Ratio	1.5	$\cdots$	$1.5\widehat{4}$	$1.\widehat{5}$	$1.571\,428$	1.6	$1.\widehat{6}$

FIG. 8. Cardiac Devil's staircase. Panel (a) shows the ratio between the number of peaks (i.e., AP and EAD peaks) vs the number of APs for detected periodic orbits when varying *PCL*, from which an ascending staircase toward the continuous EAD case can be seen. Primary steps $(1^0 (1^1)^n)$ are plotted in magenta and secondary steps in gray. The time series of the corresponding periodic orbits for several primary steps are plotted in blue, with the corresponding sequence indicated in a box. Panel (b) magnifies the final part of the staircase. Note that, even if there is a chaotic region, some stability windows with periodicity can be found inside. Panel (c) magnifies the secondary step where a two-AP periodic orbit $(1^0 1^1)$ evolves to a three-AP periodic orbit $(1^0 (1^1)^2)$.

of the type $\left(1^0(1^1)^m\right)^n \left(1^0(1^1)^{m+1}\right)$, where $n = 1$ corresponds to the highest secondary step and, as n increases, the intermediate secondary steps go down in the staircase.

From Fig. 8(a), it can be noted that the further we climb on the primary stair, the smaller the secondary (and primary) steps. And, in the jumps between primary steps, the further we go down within that jump, the smaller the secondary steps, which makes it increasingly difficult to achieve a high level of detail. In any case, the combination of these two notations (using parameters n and m) provides us with the two patterns of evolution of the periodic orbits in both the primary and secondary stairs that compose the complete evolution from the orbit 1^0 formed by a single AP not having EAD to the 1^1 orbit formed by a single AP that always has an EAD. In Sec. V, this evolution will be shown not to be a singularity, but to be reproduced in a wide region of the parameter space.

V. MULTIPARAMETRIC BIFURCATION ANALYSIS

Of the 177 parameters of the 27D Sato model, some of them have been reported to have the largest influence on model dynamics based on a sensitivity analysis.[7] To carry out a preliminary study on the influence of some parameters in the generation of EADs, we selected PCL as the main parameter and two additional parameters, K_{mNao} and K_j, identified from the sensitivity study performed in Ref. 7. K_{mNao} is the extracellular sodium dissociation constant used to calculate the I_{NaCa} current and, in turn, update sodium and calcium concentrations. K_j is the threshold for leak onset used to calculate the SR leak flux J_{leak}, which serves to update free Ca^{2+} in the cytosol and in the SR. Note that this selection of parameters is done to show that the border of the region of EADs is present in different parametric regions, while a more biologically oriented and comprehensive analysis is part of our future research work.

We first performed the analysis of the biparametric region with $PCL \in [1000, 1500]$ ms and $K_{mNao} \in [40, 270]$ mM. As the default value of K_{mNao} is 87.5 mM, the variation goes from -50% to 300% of that value. Since the bifurcation diagram cannot be plotted in the biparametric representation, the ratio between the number of AP and EAD peaks per orbit and the number of APs is represented to identify regions with different amounts of APs with and without EADs. Figure 9(a) shows the biparametric diagram representing the mentioned ratio in the color scale shown on the left. The horizontal green line, in the lower part of diagram, corresponds to the standard value $K_{mNao} = 87.5$ mM. As can be observed from the diagram, the uniparametric evolution described in previous sections, obtained by varying PCL while keeping $K_{mNao} = 87.5$ mM (default value), is very similar to those obtained for any other fixed value of K_{mNao} as long as such a value is lower than ≈ 170 mM (almost double the standard value). The only observable difference is that bifurcations occur at slightly lower PCL values when K_{mNao} is higher than the default value.

Figure 9(d) shows the default bifurcation diagram [Fig. 3(a)] with identification of the transitions, which are associated with the boundaries between regions marked in colors in the biparametric diagram. In the upper part of the diagram, corresponding to values of K_{mNao} higher than 170 mM, the transitions can be seen to differ

from those analyzed for the lower part. The horizontal green line for $K_{mNao} = 200$ mM is associated with the bifurcation diagram shown in panel (b). As can be seen, the global structure in this line is similar: low PCL values cause the system to have a periodic orbit with a single AP that does not have an EAD; for intermediate PCL values, around 1200 ms, there is a periodic orbit of the type $1^0 1^1$; and, starting at 1400 ms the periodic orbit has a single AP with an EAD. Note that there is also a very small coexistence region on the left part of plot (b) in the transition from non-EAD to EAD, similarly to the line $K_{mNao} = 87.5$ mM, but in this case it seems it has almost disappeared. The main differences for distinct K_{mNao} values are seen in the transitions between the three main states, whose analysis is out of the scope of this study. Panel (c) shows the bifurcation diagram corresponding to the magenta vertical line in panel (a). In this case, the value of $PCL = 1282$ ms remains fixed and K_{mNao} is the bifurcation parameter (increasing values in blue and decreasing values in red). Panel (c1) shows an enlargement of the area in which EADs begin to appear. In this case, coexistence is no longer detected in the transition. This fact means that the bistability phenomenon appears only when the non-EAD to EAD transition occurs for lower values of K_{mNao}. Panel (c2) shows a magnification of the lower area with the existing transitions between the periodic orbits $1^0 1^1$ and $1^0(1^1)^2$. High similarity between this bifurcation diagram and the one shown in Fig. 6(a) can be observed.

By moving from left to right, or vice versa, and from bottom to top, or viceversa, in the upper part of Fig. 9(a), the four panels of Fig. 10 were obtained. The bottom right panel corresponds to the upper part of Fig. 9. Globally, no major differences are observed among the four panels. However, by looking to the interior of the discontinuous rectangle on the left side of each panel, it can be seen that, for the same parameter values, different dynamics are detected corresponding to the previously described bistability when passing from the 1^0 orbit to the $1^0 1^1$ orbit, in this case identifying an approximately triangular region of coexistence. Furthermore, by looking at the interior of the other discontinuous rectangle (further to the right), it can be seen how the (almost vertical) stripes from yellow to orange show different thicknesses in the different panels. These four pictures indicate that the coexistence detected in Fig. 6 remains (with slight variations) up to K_{mNao} values close to 180 mM. Other smaller coexistence regions may also exist but they are difficult to detect at this scale.

Next, the three-parameter phase space defined by considering PCL, K_{mNao}, and K_j as free parameters was analyzed. In Fig. 11, a 3D composition image is presented, in which different biparametric diagrams like the one shown in Fig. 9(a) but for different K_j values (10, 50, 150, and 250 μM) are shown. The normal beat, that is, the 1^0 periodic orbit (ratio = 1), is not colored and, therefore, only the region with EADs (*the EAD parametric volume*) is presented. Since the default value of K_j used in previous analysis is 50 μM, the second horizontal diagram starting from the bottom coincides with part of the results shown in Fig. 9(a). As can be observed from Fig. 11, the changes produced by varying K_j are minimal. There is only a slight displacement of the area of EAD appearance when K_j is increased. This can be better visualized by looking at the magenta line, which passes through the point with the lowest PCL value on each horizontal plane and it can be seen to have some inclination. Nevertheless, it should be taken into account that K_j has a large variation, as the
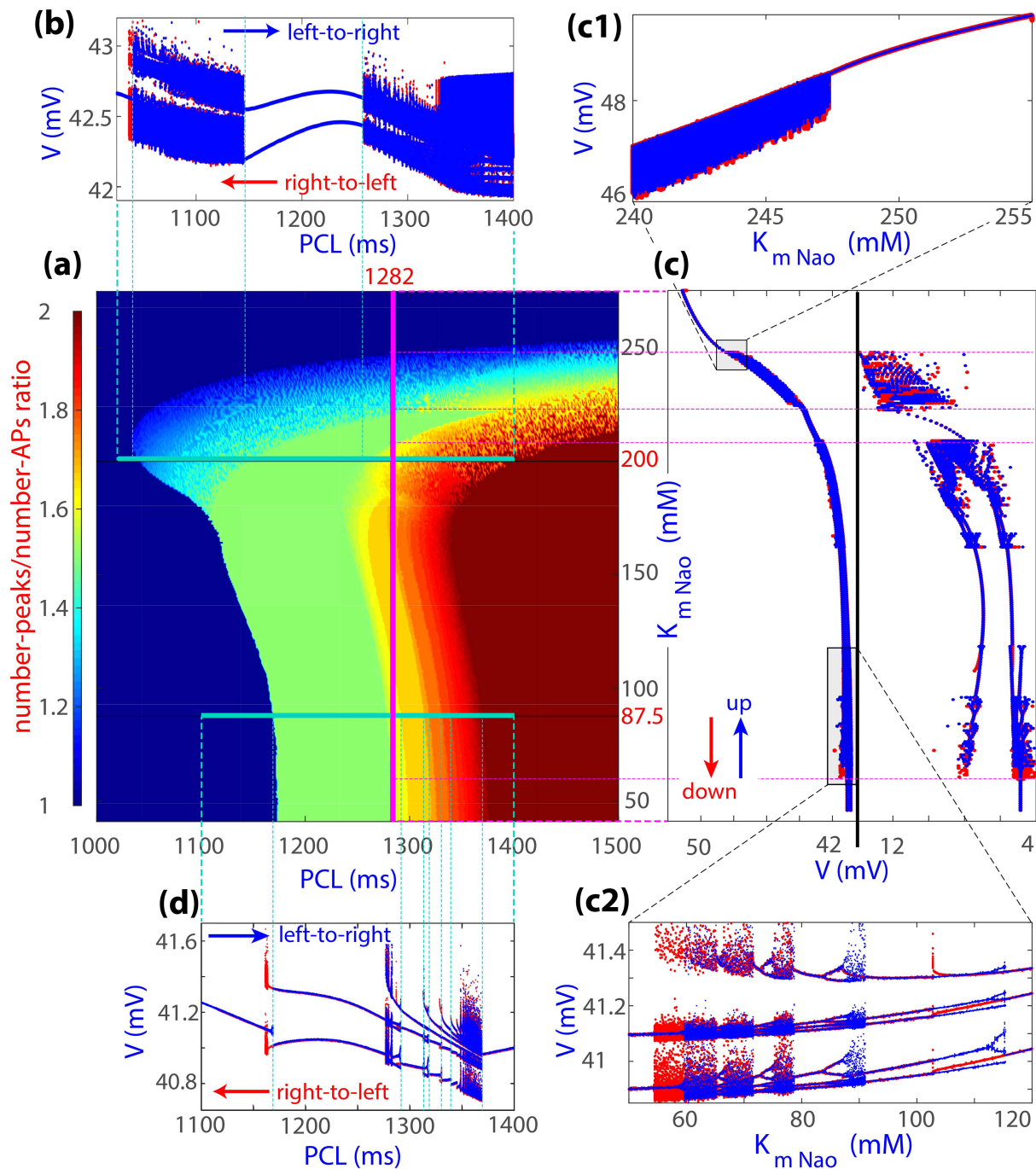
FIG. 9. (a) Biparametric bifurcation diagram considering *PCL* and K_{mNao} as free parameters. Color code represents the ratio between the number of (AP and EAD) peaks and the number of APs. The horizontal green line in the lower part corresponds to the default value of $K_{mNao} = 87.5$ mM, for which the uniparametric bifurcation diagram is shown in panel (d) (see Figs. 2–6 for more detailed diagrams). In the upper part of panel (a), the horizontal green line corresponds to another value of $K_{mNao} = 200$ mM, far from the standard value, with the corresponding uniparametric bifurcation diagram shown in panel (b). The vertical magenta line corresponds to the fixed value $PCL = 1282$ ms, for which the corresponding uniparametric bifurcation diagram is shown in panel (c) divided into the upper and lower AP peaks. In this case, the free parameter is K_{mNao} (increasing values in blue and decreasing values in red). In panel (c1), magnification of the transition region from no EADs to EADs is shown, with no coexistence observed. In (c2), the transition region from $1^0 1^1$ to $1^0 (1^1)^2$ periodic orbits is enlarged.
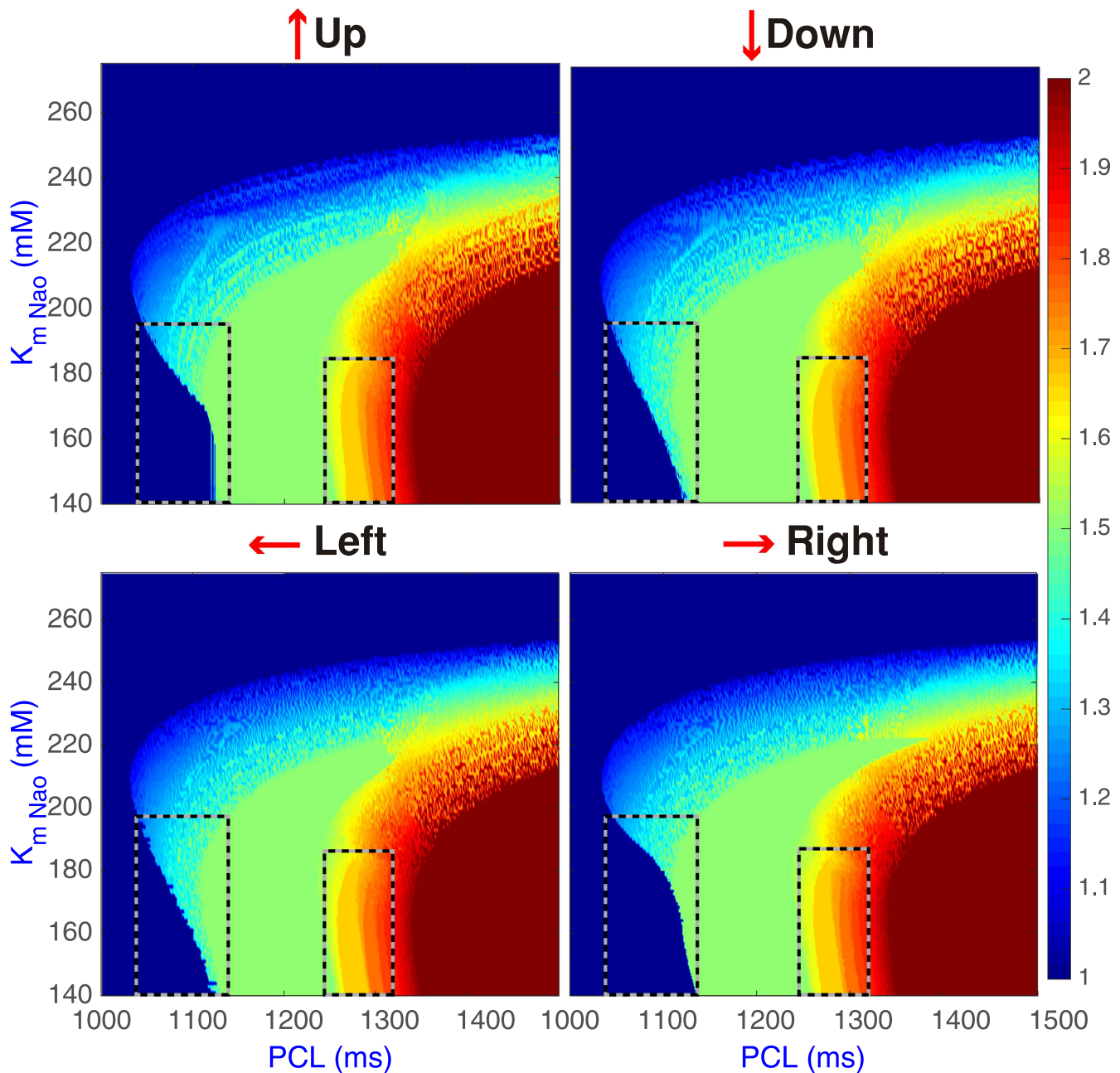
FIG. 10. Biparametric bifurcation diagrams with different continuation strategies (directions of travel along the horizontal or vertical lines that form the mesh). Each strategy determines the initial conditions considered for each diagram. In the "up" and "down" plots, vertical lines are followed (fixing *PCL* value and varying K$_{mNao}$); in the "left" and "right" plots, horizontal lines are followed (fixing K$_{mNao}$ value and varying *PCL*). Distinctive regions are marked with dashed rectangles. The "right" plot corresponds to the upper part of Fig. 9(a).

upper horizontal diagram corresponds to $K_j = 250\,\mu$M, that is, five times its default value.

The vertical biparametric diagram in Fig. 11 can also be seen in panel (b). The colored stripes, which indicate the different ratios of

APs with EADs in the attractor, are almost vertical. This illustrates the low global influence that K_j has on the general dynamics of the system, but, as some inclination is present, there is always a cross point that, for specific intervals of variation, could be relevant. In
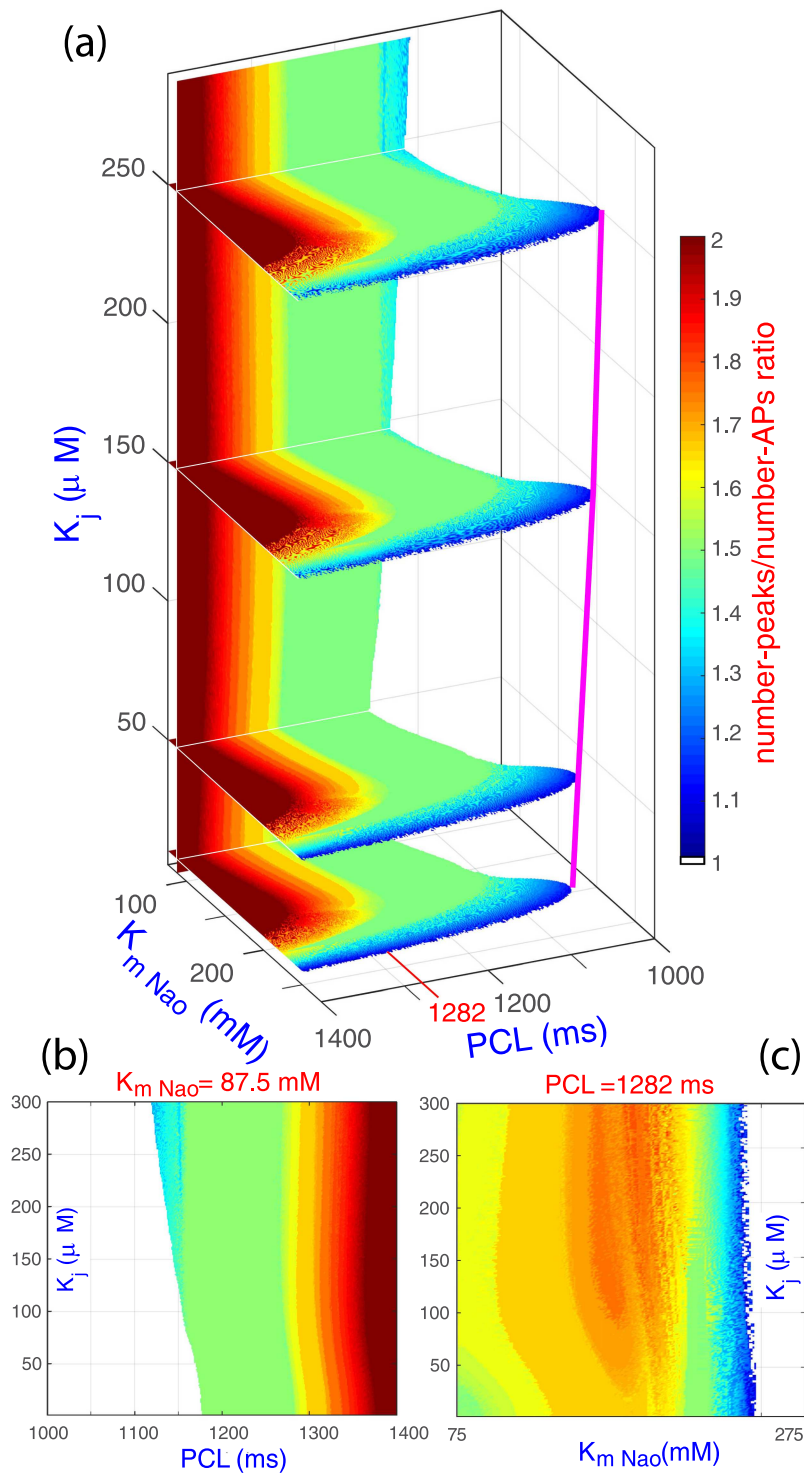
FIG. 11. (a) Three-parameter (PCL, K_{mNao}, K_j) diagram using the same color code as in Figs. 9(a) and 10, with the exception of dark blue (1^0 periodic orbit), which has been removed and, thus, only the region with EADs (*the EAD parametric volume*) is presented. Magenta line marks the beginning of the EAD appearance region. (b) Biparametric (PCL, K_j) diagram for the default value $K_{mNao} = 87.5$ mM. (c) Biparametric (K_{mNao}, K_j) diagram by setting $PCL = 1282$ ms.

panel (c), *PCL* is set to 1282 ms while K_j and K_{mNao} are left free. The selected plane is vertical and perpendicular to all the planes in panel (a), but, due to the particular choice of the *PCL* value, it also passes through the border area between several consecutive transitions seen in Fig. 6. This means that, in this case, changing the value of K_j in the central area of the diagram may originate large changes in the system dynamics. It should be noted that it is a direct consequence of the particular selection of the *PCL* value close to a transition area. For another *PCL* value like *PCL* = 1200 ms, panel (c) would have been all green except for large values of K_{mNao}. Similarly happens with K_{mNao} unless values above 170 mM are considered. Overall, with the exception of *PCL*, which always has a high influence on the system dynamics, the other two parameters here studied will only have an important influence in cases near a transitional border. Future work should aim at determining the influence of the different model parameters on system dynamics to elucidate the phenomena the model can reproduce.

VI. DISCUSSION

In this study, we analyze the dynamics of the 27D Sato model[8] as given in Ref. 7. 2D and 3D parametric simulations are performed and bifurcation diagrams and peak-counting techniques are used to analyze EAD generation as a function of *PCL* and two other model parameters. First, we show the presence of bistable

regimes, in agreement with findings from other experimental and computational cardiac investigations[13,41,42] showing the presence of bistability and hysteresis phenomena. However, in the literature, there is a lack of detailed multiparametric analysis. Here, we show that one of the processes to change from APs with no EADs to APs with EADs goes through an intermediate state presenting alternans, i.e., an AP without an EAD followed by another AP with an EAD. This means that the system goes from a 1^0 configuration of the periodic orbits to a $1^0 1^1$ configuration and finally the process ends on a periodic orbit with every AP having an EAD (1^1). In between, the cardiomyocyte dynamics presents more and more APs with EADs following a cardiac Devil's staircase (Sec. IV).

Of the investigated model parameters, the dependence of system dynamics on *PCL* is in line with previous studies, particularly using the same Sato model.[8] While it is already reported in the literature that the higher *PCL*, the more EADs can be observed, the transition from non-EADs to EADs in all APs is not fully described and the number of APs with EADs that are added to the periodic behavior is not quantified. Besides *PCL*, other model parameters and variables used in the computation of intracellular calcium and sodium concentrations are shown in the literature[13,39] to additionally have a role in the generation of EADs. From our results in Sec. V and, in particular, from Figs. 9 and 11, we can conclude that, although the influence of *PCL* is more evident, there are intervals of variation in other parameters for which the same change
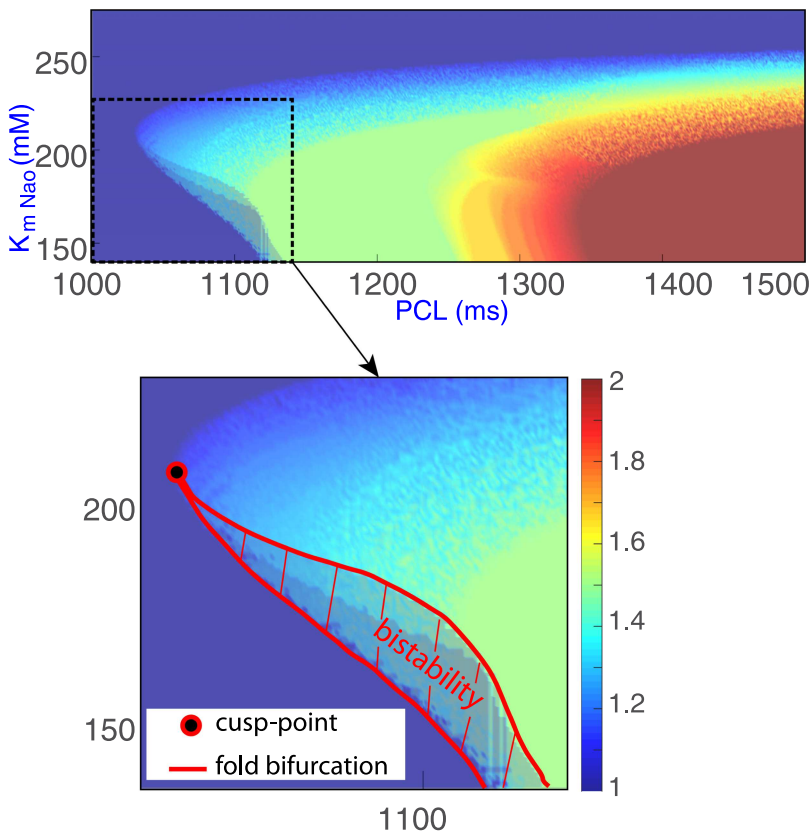

FIG. 12. Overlapping of the four plots of Fig. 10 to locate the main bistability region. A magnification is shown in the bottom panel with the approximate location of the fold bifurcation curves that limit the bistability region and a conjectured cusp codimension-two bifurcation point.

from non-EADs to EADs is present. This confirms the need for a multiparametric analysis.

A major question relates to the dynamics of the process. Although analytical techniques cannot be used due to the high dimension of the model, from our results of the uniparametric bifurcation diagram (see Fig. 3), different transitions are identified. On the one hand, the transition from non-EADs to EADs and, on the other hand, the transition from n APs with EADs to $n + 1$ APs with EADs. In the first case, the transition could be produced by a torus bifurcation of the orbit without EAD (Fig. 4), although other mechanisms giving rise to the formation of two or more loops in the orbit (like a period-doubling bifurcation) would also be possible.[33,34] The torus bifurcation is related to the process of generation of an invariant two-dimensional torus from a periodic orbit (this process is also called the Neimark-Sacker bifurcation[43] in the Poincaré map of a limit cycle in ODE). This mechanism has been observed in other biological models.[44] Furthermore, in the region of creation of the EAD, there is bistability of an AP without EAD and alternans of an AP without EAD and an AP with an EAD. To study this process in a biparametric space, the four biparametric plots of

Fig. 10 can be superimposed to approximately locate part of the bistability region. It should be noted that these four subplots correspond to different initial conditions and are similar in most areas except for the transition regions due to the bistability phenomena. Their superposition is shown in Fig. 12. In the top panel, EAD development from left to right (i.e., by increasing PCL) is shown, with different blue colors due to the differences in the limit of the non-EAD–EAD behavior of the four subplots. The bottom panel shows a magnification of the top one, where the bistability region is approximated by adding two red curves. These curves are conjectured as fold (saddle-node) bifurcations of limit cycles, giving rise to the phenomenon of hysteresis, which is typical of dynamical systems. Putting everything together (Figs. 4 and 12), we conjecture that one of the possible mechanisms for EAD generation is by means of the creation of a hysteresis loop, due to the existence of two fold bifurcations, with two stable branches (one without and another one with EADs) and an unstable orbit in between, as shown in Fig. 13(a).

Still the question on how to connect Figs. 4 and 12 needs to be addressed. From Fig. 12, the fold bifurcations seem to connect each
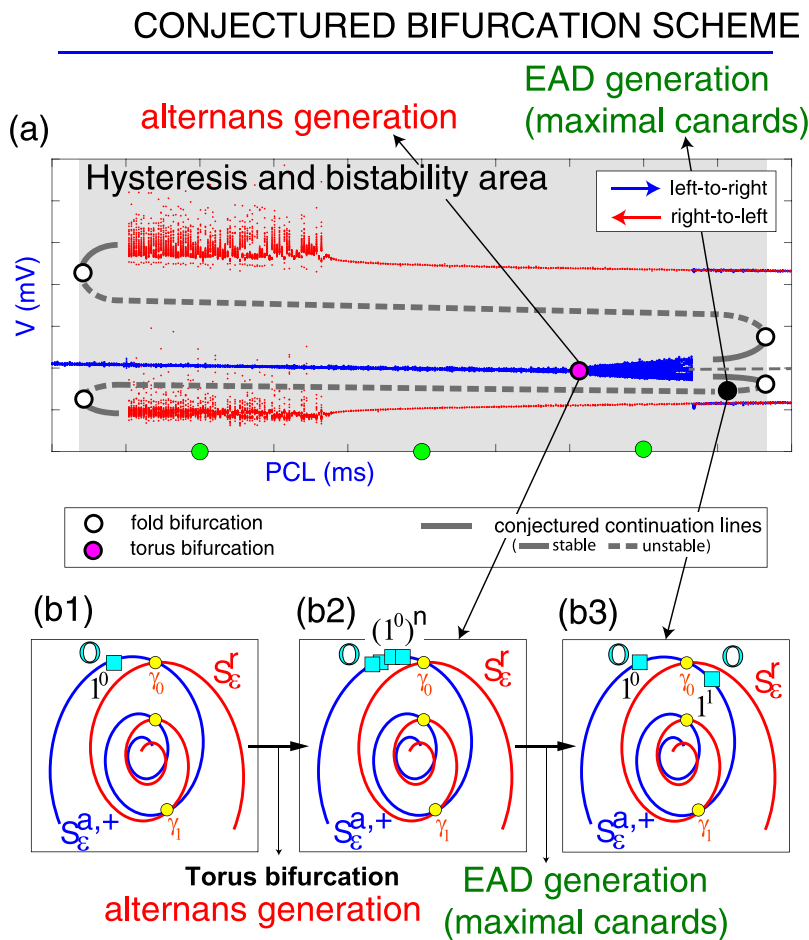
FIG. 13. Theoretical explanation of the mechanism that results in EAD development. (a) Conjectured hysteresis loop delimited by twofold bifurcations is shown using the data from Fig. 4 and the conjectured results from Fig. 12. [(b1)–(b3)] Conjectured process of EAD generation in some APs of the alternans created on a torus bifurcation. A theoretical scheme of one bidimensional section of the slow manifolds (attractive $S_\varepsilon^{a,+}$ in blue and repulsive S_ε^r in red), the maximal canards γ_i (yellow dots), and the hypothetical location of the different APs of the orbit O (blue squares) are shown. Following Ref. 17, the maximal strong canard γ_0 would organize the EADs.

other at a value K$_{mNao}$ $\approx$ 207, which gives rise to a cusp bifurcation (a codimension-two bifurcation point). For higher K_{mNao} values, fold bifurcations and hysteresis are no longer present, as shown at the vertical slice (PCL = 1282 ms) of Figs. 9(c) and 9(c1) where no bistability is shown in the upper part. Also, in Fig. 9(b), the bistability region is very small due to the proximity (K$_{mNao}$ = 200) of the cusp point.

Finally, we address how and where EADs are created. Although the detailed process of EAD development is an open problem in the literature, some new dynamical system explanations have been recently introduced using low-dimensional models[16–18,39,45,46] where a new fast-slow decomposition of the models (two-slow one-fast rather than two-fast one-slow) allows to identify the key role of maximal canards on the creation of EADs (for more details on canard generation and theory, see Refs. 16, 17, and 39). We observe that in many models the canard phenomenon has made it possible to describe and explain the generation of additional peaks, as in the neuron models.[47,48] From these studies, the number of EADs is related to the number of maximal canards the orbit crosses. As shown in Ref. 17, the local twisting of the slow manifolds gives rise to a finite number of intersections of the different sheets (attractive $S_\varepsilon^{a,+}$ and repulsive S_ε^r), which are called maximal canards.[30] The first intersection is in fact the maximal strong canard γ_0 and is the limit between orbits that exhibit or not EAD near the folded node. On one side of γ_0, the orbit does not have EADs while on the other side it does. If there are more intersections (γ_1, γ_2,...), more EADs are allowed, but, for our parameter plane, only one EAD is detected and, thus, only one of those intersections is assumed to be present. Based on our simulations using the 27D Sato model and using the low-dimensional results shown in Ref. 17, we can conjecture the theoretical scheme of the creation of the EAD. First, a torus bifurcation occurs, which allows the creation of alternans and an orbit with different APs. Moving on the bifurcation line, some of the APs of the orbit cross the maximal strong canard γ_0, then these APs start to create an EAD and the orbit goes from the 1^0 configuration (ratio 1) toward the $1^0 1^1$ configuration (ratio 1.5). This process is shown in plots (b1), (b2), and (b3) of Fig. 13. Note that the proposed theoretical scheme is a conjectured one, but it is based on all our results and the recent theoretical insights on simpler models. Its full description is an open problem and it is part of our current work.

The ionic mechanisms underlying the transition from non-EADs to EADs or from n APs with EADs to $n + 1$ APs with EADs require further investigation. Multiple ionic currents and concentrations may be involved in the EADs observed here when pacing the cardiomyocyte at low frequencies. Nevertheless, the I_{Ca} current seems to play a major role in our simulations, as confirmed by the fact that inhibiting this current, even to only modest extents, precluded EAD formation. Other currents, including the inward current through the sodium-calcium exchanger, were not as relevant as I_{Ca}. Drugs commonly employed to block calcium channels also reduce the calcium influx required for excitation–contraction coupling. Thus, other interventions designed to target the specific mechanisms underlying EAD generation while preserving contraction should be investigated in future studies. Such I_{Ca}-directed interventions could range from modulation of the slope of voltage-dependent channel activation and inactivation, the time constants

of channel gating or the magnitude of the late (or pedestal) I_{Ca} current.[49,50] A detailed analysis on the impact of such potential ionic mechanisms in the processes investigated in this study will be conducted as part of future research work.

VII. CONCLUSIONS

The parametric space of a 27D cardiac cell model proposed by Sato *et al.*[6] is analyzed. By combining different numerical techniques, the one-parameter, two-parameter, and three-parameter phase space are presented using PCL and two other model parameters related to calcium and sodium concentrations as bifurcation parameters. Different behaviors such as bistability, chaotic attractors, and various bifurcations are identified. Using the ratio between the number of voltage peaks and the number of APs, a *cardiac Devil's staircase* is presented that illustrates, in a discrete way, the symbolic process of changing from absence of EADs to full presence of EADs in all beats. Interestingly, our results show that there is a limit in the parameter space between APs without EADs and APs with EADs, with this limit being present in all studied parameters. In the transition area from AP without to AP with EAD, it is possible to observe that, for the most biologically relevant parametric region, the change is organized by a hysteresis loop that generates two stable orbits, with and without EAD. This bistability has been previously observed in the literature but, here, it is related to the existence of twofold bifurcations and a cusp bifurcation point that establishes the maximum value of the parameter where bistability can be expected. In addition, our simulations point out that previously there is alternans generation by a torus bifurcation. We conjecture that this splitting of the orbit helps in the EAD creation process, as it allows some of the APs to cross the region where EAD is promoted. We also link this process to the recently reported phenomenon of maximal canards in the fast-slow decomposition of low-dimensional cardiomyocyte models and, as a conclusion, we propose a conjecture that gives a theoretical scheme of the EAD generation process in the Sato cardiomyocyte model.

DATA AVAILABILITY

The data that support the findings of this study are available within the article.

REFERENCES

[1] C. T. January and J. M. Riddle, Circ. Res. **64**, 977 (1989).

[2] Y. Song, J. C. Shryock, and L. Belardinelli, Am. J. Physiol. Heart Circ. Physiol. **294**, 2031 (2008).

[3] L.-H. Xie, F. Chen, H. S. Karagueuzian, and J. N. Weiss, Circ. Res. **104**, 79 (2008).

[4] C. Antzelevitch and S. Sicouri, J. Am. Coll. Cardiol. **23**, 259 (1994).

[5] R. B. Huffaker, J. N. Weiss, and B. Kogan, Am. J. Physiol. Heart Circ. Physiol. **292**, 3089 (2006).

[6] D. Sato, L.-H. Xie, A. A. Sovari, D. X. Tran, N. Morita, F. Xie, H. Karagueuzian, A. Garfinkel, J. N. Weiss, and Z. Qu, Proc. Natl. Acad. Sci. U.S.A. **106**, 2983 (2009).

[7] S. Otte, S. Berg, S. Luther, and U. Parlitz, Commun. Nonlinear Sci. Numer. Simul. **37**, 265 (2016).

[8] D. Sato, L.-H. Xie, T. P. Nguyen, J. N. Weiss, and Z. Qu, Biophys. J. **99**, 765 (2010).

[9] R. Madhvani, Y. Xie, A. Pantazis, A. Garfinkel, Z. Qu, J. Weiss, and R. Olcese, J. Physiol. **589**, 6081 (2011).

[10] C. Napolitano, S. Priori, P. Schwartz, R. Bloise, E. Ronchetti, J. Nastoli, G. Bottelli, M. Cerrone, and S. Leonardi, JAMA **294**, 2975 (2005).

[11] J. Weiss, A. Garfinkel, H. Karagueuzian, P.-S. Chen, and Z. Qu, Heart Rhythm **7**, 1891 (2010).

[12] Z. Qu and J. Weiss, Annu. Rev. Physiol. **77**, 29 (2014).

[13] Y. Xie, Z. Liao, E. Grandi, Y. Shiferaw, and D. M. Bers, Circ. Arrhythm. Electrophysiol. **8**, 1472 (2015).

[14] Z. Qu, G. Hu, A. Garfinkel, and J. N. Weiss, Phys. Rep. **543**, 61 (2014).

[15] D. Sato, C. E. Clancy, and D. M. Bers, Heliyon **3**, e00388 (2017).

[16] P. Kügler, A. H. Erhardt, and M. Bulelzai, PLoS One **13**, e0209498 (2018).

[17] T. Vo and R. Bertram, Phys. Rev. E **99**, 052205 (2019).

[18] R. Barrio, M. A. Martínez, L. Pérez, and E. Pueyo, Mathematics **8**, 880 (2020).

[19] J. Rinzel, in *Mathematical Topics in Population Biology, Morphogenesis and Neurosciences: Proceedings of an International Symposium held in Kyoto, November 10–15, 1985*, edited by E. Teramoto and M. Yumaguti (Springer, Berlin, 1987), pp. 267–281.

[20] D. X. Tran, D. Sato, A. Yochelis, J. N. Weiss, A. Garfinkel, and Z. Qu, Phys. Rev. Lett. **102**, 258103 (2009).

[21] D. R. Chialvo, R. F. Gilmour, and J. Jalife, Nature **343**, 653 (1990).

[22] A. Vinet, D. R. Chialvo, D. C. Michaels, and J. Jalife, Circ. Res. **67**, 1510 (1990).

[23] X. Huang, Z. Song, and Z. Qu, PLoS Comput. Biol. **14**, e1006382 (2018).

[24] B. P. Damiano and M. R. Rosen, Circulation **69**, 1013–1025 (1984).

[25] A. L. Hodgkin and A. F. Huxley, J. Physiol. **117**, 500 (1952).

[26] T. R. Shannon, F. Wang, J. Puglisi, C. Weber, and D. M. Bers, Biophys. J. **87**, 392 (2004).

[27] A. Mahajan, Y. Shiferaw, D. Sato, A. Baher, R. Olcese, L.-H. Xie, M.-J. Yang, P.-S. Chen, J. G. Restrepo, A. Karma, A. Garfinkel, Z. Qu, and J. N. Weiss, Biophys. J. **94**, 392 (2008).

[28] A. Mahajan, D. Sato, Y. Shiferaw, A. Baher, L. Xie, R. Peralta, R. Olcese, A. Garfinkel, Z. Qu, and J. Weiss, Biophys. J. **94**, 411 (2008).

[29] Y. Shiferaw, M. Watanabe, A. Garfinkel, J. Weiss, and A. Karma, Biophys. J. **85**, 3666 (2003).

[30] M. Desroches, J. Guckenheimer, B. Krauskopf, C. Kuehn, H. M. Osinga, and M. Wechselberger, SIAM Rev. **54**, 211 (2012).

[31] A. Wolf, J. B. Swift, H. L. Swinney, and J. A. Vastano, Physica D **16**, 285 (1985).

[32] S. Bauer, G. Röder, and M. Bär, Chaos **17**, 015104 (2007).

[33] E. M. Cherry, Chaos **27**, 093902 (2017).

[34] C. M. Berger, X. Zhao, D. G. Schaeffer, H. M. Dobrovolny, W. Krassowska, and D. J. Gauthier, Phys. Rev. Lett. **99**, 058101 (2007).

[35] C. Grebogi, E. Ott, and J. A. Yorke, Nucl. Phys. B, Proc. Suppl. **2**, 281 (1987).

[36] S. Serrano, M. A. Martínez, and R. Barrio, Chaos **31**, 043108 (2021).

[37] P. Bak, Phys. Today **39**, 38 (1986).

[38] D. R. Chialvo, D. C. Michaels, and J. Jalife, Circ. Res. **66**, 525 (1990).

[39] J. Kimrey, T. Vo, and R. Bertram, SIAM J. Appl. Dyn. Syst. **19**, 1701 (2020).

[40] E. Pueyo, A. Corrias, L. Virág, N. Jost, T. Szél, A. Varró, N. Szentandrássy, P. P. Nánási, K. Burrage, and B. Rodríguez, Biophys. J. **101**, 2892 (2011).

[41] A. R. Yehia, D. Jeandupeux, F. Alonso, and M. R. Guevara, Chaos **9**, 916 (1999).

[42] K. Tsumoto, Y. Kurata, K. Furutani, and Y. Kurachi, Sci. Rep. **7**, 10771 (2017).

[43] Y. A. Kuznetsov, *Elements of Applied Bifurcation Theory*, 3rd ed. (Springer-Verlag, New York, 2004), Vol. 112.

[44] H. Ju, A. B. Neiman, and A. L. Shilnikov, Chaos **28**, 106317 (2018).

[45] A. H. Erhardt, Processes **7**, 1 (2019).

[46] J. Kimrey, T. Vo, and R. Bertram, PLoS Comput. Biol. **16**, e1008341 (2020).

[47] G. Innocenti, A. Morelli, R. Genesio, and A. Torcini, Chaos **17**, 043128 (2007).

[48] R. Barrio, S. Ibáñez, L. Pérez, and S. Serrano, Commun. Nonlinear Sci. Numer. Simul. **83**, 105100 (2020).

[49] R. Madhvani, M. Angelini, Y. Xie, A. Pantazis, S. Suriany, N. Borgstrom, A. Garfinkel, Z. Qu, J. Weiss, and R. Olcese, J. Gen. Physiol. **145**, 395 (2015).

[50] Y. Markandeya and T. Kamp, J. Gen. Physiol. **145**, 475 (2015).